UiT
THE ARCTIC
UNIVERSITY
OF NORWAY

Faculty of Science and Technology
Department of Physics and Technology

Arctic Thin Sea Ice Thickness Regression Models For Sentinel-2

Øystein Fredriksen Skogvold

FYS-3931 Master's thesis in space physics 30 SP

May 2019

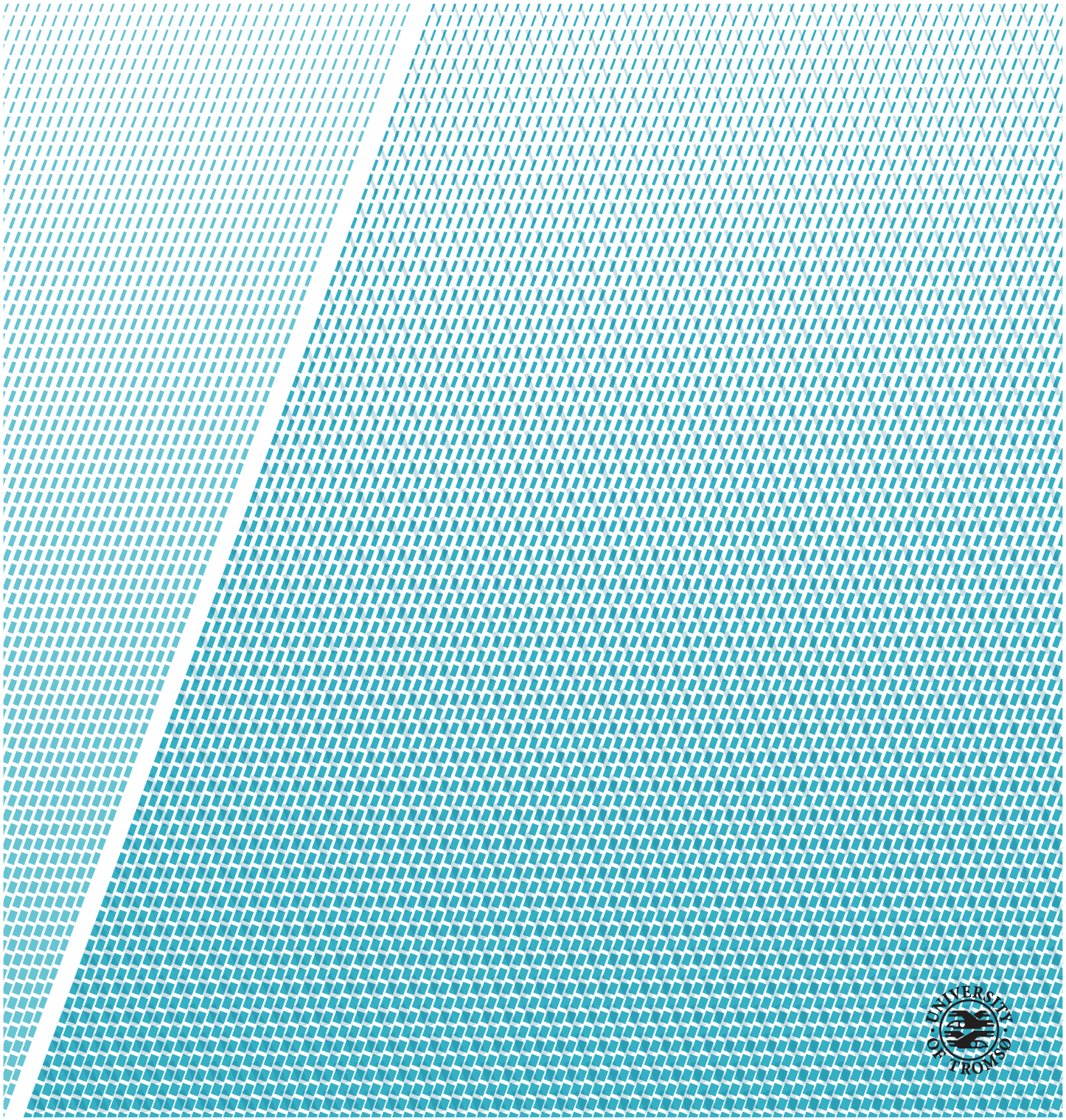

Abstract

Sea ice thickness is an important parameter for modelling the sea ice mass balance, momentum and gas exchanges, and global energy budget. The interest of studies into thin sea ice has increased as trends in recent years show a increasing abundance in thin first year ice. Existing thin sea ice thickness products operate at resolutions down to 750 meters. Very high resolution (less than 100 meters) retrieval of sea ice parameters is of particular interest due to maritime navigation and model parametrization of physical processes at meter-scaled resolutions that usually requires in-situ measurements.

The Norwegian Meteorological Institute provided a 500 meter resolution thin sea ice thickness product developed by the Norwegian Computing Centre for the Norwegian Space Agency's "Sentinel4ThinIce" project. The product is derived from Sentinel-3's SLSTR sensor. Using overlapping multispectral optical data from Sentinel-2's MultiSpectral Instrument at metre-scaled resolutions, we retrieved multiple regression models for thin sea ice thickness for Sentinel-2 data. The models included three univariate models for three different spectral band combinations using non-linear least squares method, and one multivariate model for three different band reflectance data-sets using a gradient boosting regression tree.

The optical band reflectance data increased monotonically with sea ice thickness and saturated for thicker ice, proving a clear correlation between thin sea ice thickness and Sentinel-2's band reflectance. The multivariate model produces overall best results compared to the univariate models. The reliability of the models couldn't be trusted due to inaccurate atmospheric correction procedures and not enough temporal and geographical variance in the data-set. Proper calibration of Sentinel-2 data is of high priority in order to extend Sentinel-2's platform further into Arctic research.

Acknowledgements

First of all I want to thank my supervisor, Anthony P. Doulgeris, for supporting me through this project with a great attitude. Couldn't have done it without the help and knowledge you provided. I would like to thank my co-supervisor, Nick Hughes at MET, for providing data and resources to help guide me in the right direction.

Thanks to Vebjørn Karisari at CIRFA for helping me with the code for satellite imagery search and acquisitions. And a last big thanks to my fellow students in my office, for creating a great and encouraging working environment.

Contents

List of Figures

List of Tables

List of Abbreviations

AATSR Advanced Along-Track Scanning Radiometer

AC Atmospheric Correction

API Application Programming Interface

BOA Bottom Of Atmosphere

CRS Coordinate Reference System

DOS Dark Object Subtraction

EM Electromagnetic

EO Earth Observation

GBM Gradient Boosting Machine

IR Infrared Radiation

LST Land Surface Temperature

MET Norwegian Meteorological Institute

MSI Multi-Spectral Instrument

NIR Near-Infrared Radiation

NLLS Non-Linear Least Squares

NR Norwegian Computing Centre

RMSE Root Mean Squared Error

RS Remote Sensing

S-3 Sentinel-3

S-2 Sentinel-2

SAR Synthetic Aperture Radar

SIT Sea Ice Thickness

SLSTR Sea and Land Surface Temperature Radiometer

SRF Spectral Response Functions

SST Sea Surface Temperature

SWIR Short Wavelength Infrared Radiation

TIR Thermal Infrared Radiation

TOA Top Of Atmosphere

UV Ultra Violet

VIS Visible Radiation

WV Water Vapour

1 Introduction

This thesis evaluates the possibility of thin Sea Ice Thickness (SIT) estimation using high resolution optical satellites sensors, specifically Sentinel-2 (S-2) from ESA's Copernicus platform. With the help of the Norwegian Ice Service from the Norwegian Meteorological Institute (MET), I was able to use a in development thin SIT product retrieved from Sentinel-3 (S-3)'s Sea and Land Surface Temperature Radiometer (SLSTR) sensor at coarse resolution and combine the SIT products with co-located high resolution S-2 scenes. The thin SIT product is developed by Øystein Rudfjord and Rune Solberg at the Norwegian Computing Centre (NR), through the Norwegian Space Agency under the project, "Sentinel4ThinIce". MET are testing the code and was able to share the results. A pixel by pixel thin SIT regression model for the high resolution multi-spectral optical data from S-2 is the end goal, and a better understanding of the relationship between crucial sea ice parameters and its reflective properties.

1.1 Motivation and Background

Accurate knowledge of sea ice and its properties are crucial for weather and climate modelling. Sea Ice Thickness (SIT) distribution is an important parameter in polar seas for monitoring ocean atmosphere heat, momentum and gas exchanges and global energy budget (Melsheimer et al., 2016). Thin ice is of particular interest as trends in recent years of less multi-year ice and more first year ice implies a higher interest of quantifying and monitoring thin ice (Rudfjord et al., 2011).

There exists several Arctic SIT products retrieved from orbiting Remote Sensing (RS) instrument. An evaluation of four Arctic SIT product was conducted in (Melsheimer et al., 2016) and the highest spatial resolution available is at 750 m. The lack of very high resolution RS coverage of Arctic sea ice restricts knowledge about detailed meter-scaled sea ice surface properties. Very high resolution monitoring of sea ice will improve maritime navigation and process parametrization for models. Multispectral remote sensing may be a powerful tool for Arctic research and monitoring of sea ice. Sentinel-2 offers very high resolution multispectral optical data in the visible, NIR, and short wave infrared wavelength range, with pixel resolutions down to 10, 20 or 60 meters. Thus Sentinel-2 can used to bridge the spatial scale between in-situ observations and very high spatial resolution imagery (König et al., 2019).

The thin SIT retrieval algorithm from NR and its technical specifications could unfortunately not be shared, as the "Sentinel4ThinIce" project is still in development. However, the thin SIT is retrieved from Sentinel-3 SLSTR observations and the theoretical basis is covered in (Yu and Rothrock, 1996). As Sentinel-2 is a part of ESA's Earth observation satellite platform, Copernicus, with Sentinel-3, a potential bridge between coarse and high resolution thin sea ice thickness can be made. Strengthening the case of more research into Sentinel-2's capabilities of Arctic sea ice research.

The goal is the retrieval of a reliable thin SIT regression model from the very high resolution Sentinel-2 MSI instrument.

1.2 Outline

This thesis is divided into 8 chapters. Chapter 1 introduces the problem, motivation and goal of the thesis. Chapter 2 and 3 explains the important fundamental theory of optical and thermal remote sensing, and the theoretical background of optical and thermal properties of sea ice. Chapter 4 and 5 is the technical details regarding the satellite sensors, data specifications, area of interest and data acquisition/preprocessing. Chapter 6 and 7 covers the spectral response of the thin SIT in the optical, dark object subtraction, estimate of total albedo and the analysis and results from the regression models evaluated. Finally, chapter 8, include discussion regarding reliability of models and data, and conclusion of thesis.

2

Optical and Thermal Remote Sensing

The term Remote Sensing (RS) refers to the acquisition of information about the object or phenomenon without making physical contact. While RS is used in many different fields including Earth sciences, military, economy, natural disaster surveying etc. Our usage of the term RS refers to the usage of usually orbiting satellites equipped with sensors to detect and classify different objects/surface types on Earth.

2.1 Electromagnetic Energy

Interpretation and analysis of RS data is hugely dependent on a proper understanding Electromagnetic (EM) radiation and its interaction with Earths surface and atmosphere. In our case, the optical and thermal radiation refers to some portions of the whole EM spectrum that carries its own properties related to reflected radiation (optical) and emitted radiation (thermal).

2.1.1 Electromagnetic energy and the EM spectrum

EM radiation can be represented in two ways, by oscillating waves or radiant energy. The EM radiation energy is derived from oscillating magnetic and electrostatic fields that is transmitted with a velocity of the speed of light, c.

EM radiation carries the same properties as a sine wave:

$$A \cdot \sin(\frac{2\pi}{\lambda}x + \phi)$$

Where the wavelength, λ, is an important parameter differentiating the different types of EM radiation. The wavelength is related to the frequency, ν,

$$\lambda = \frac{c}{\nu} \tag{2.1}$$

The amplitude, A, is the peak value of the wave. The larger the amplitude, the higher the energy of the wave. The phase, ϕ, expresses the fraction the start point differs from the origin of the wave. Amplitude, and phase are important parameters for active sensors, like Synthetic Aperture Radar (SAR), that has all the information from the outgoing signal and can extract surface properties by looking at the difference between outgoing and incoming surface scattered signal. However, the more useful properties for our case, using passive RS sensors, comes from particle theory. EM radiation can be explained as a succession of discrete packets of energy, commonly known as photons. The amount of energy, Q, held by a single photon is related to a specific wavelength:

$$Q = h \cdot \nu = h \cdot \frac{c}{\lambda} \tag{2.2}$$

Where h is the Planck's constant. Equation 2.2 states that the shorter the wavelength, or higher the frequency, more energy is carried per photon.

As previously mentioned the different types of EM radiation is defined by its wavelength or frequency. We call the total range of wavelengths of EM radiation the EM spectrum (see Fig. 2.1). The different portions of the EM spectrum are referred to by name, where each portion represent a range of wavelengths. The portions of the EM spectrum that we will consider are:

- **Visible Radiation (VIS)** (380nm to 740nm): The portion of the EM spectrum that is visible to the human eye, ranging from short wave blue/violet light (400 - 490nm) to red light (635 - 700nm).

- **Infrared Radiation (IR)** (700nm to 1mm): Radiation beyond the visible red light towards longer wavelengths. IR includes several major subdivisions important for RS:

  - *Near-Infrared Radiation (NIR)* (0.7-1.2 μm): Useful for discriminate vegetation types.

  - *Short Wavelength Infrared Radiation (SWIR)* (1.3-3 μm): Used for monitoring surface features at night.

  - *Thermal Infrared Radiation (TIR)* (3 μm and longer): Area responsible for the sensation of "heat". Earths thermal emission has a peak at around 10 μm. Also useful for retrieving surface temperature.

Before we go more into detail about the principle physical properties from optical and thermal radiation, we need to know more about the RS relevant interactions with atmosphere.

2.1.2 Energy interactions with atmosphere

Before the EM radiative energy can reach Earth's surface, it has to pass Earth's atmosphere. The solar radiation is subjected to several interactions in the atmosphere, two major interactions are:

- **Absorption** of radiant energy in certain wavelengths. This causes limitations for RS instruments to sense only those spectral regions where absorption is minimal. Tied with transmission.

- **Scattering** and reflection of radiant energy. Alters the EM waves' path and intensity.

Absorption in the atmosphere occurs when EM energy travelling through is partly absorbed by various atmospheric molecules. Some prominent efficient absorbers of EM radiation are O_3 (ozone), H_2O (Water Vapour (WV)), and CO_2 (carbon dioxide). Figure 2.2 gives a representation of the atmospheric transmission in the IR (0 to 15 μm) wavelength range. The atmosphere behaves as a selective filter at different wavelengths, commonly known as atmospheric transmission windows, giving us the useful wavelength ranges for RS applications.
Scattering is the redirection of EM energy by particles, large molecules or atmospheric gases in the atmosphere. The amount of scattering in the atmosphere depends on several factors including the wavelength of the incident radiation, the density of particles and gases, the size of the particles and molecules, and the distance that the EM radiation propagates through atmospheric column. The effect of scattering of incident solar radiation in the Earth's atmosphere is that a portion of the radiation is redirected back towards space, or towards the Earth's surface. There are three main contributing components of atmospheric scattering, the most common and major one is known as *Rayleigh scattering*. Rayleigh scattering occurs when the wavelength of the incident solar radiation is very long relative to the diameter of atmospheric particles. The amount of light scattered in this fashion is inversely proportional to the fourth power of the wavelength (Barnett, 1942). Meaning that blue light in the VIS region with a shorter wavelength is scattered significantly more than red light. *Mie scattering* is the second major contributor and is caused by larger particles, including dust, pollen, smoke and water droplets. The diameter of these par-

ticles are roughly the equivalent to the wavelength of the incident radiation. Mie scattering is wavelength dependent, but the shape and composition of the atmospheric particles are important in the analysis. The last scattering mechanism is called *non-selective scattering*, and is caused by particles much larger than the incident radiation, it's not wavelength dependent and scatters all visible light equally, so we observe it as gray-ish haze.
Radiation sensed from outside the atmosphere is a mix of reflected, emitted and re-radiated radiation from both the surface and atmosphere. There exists many atmospheric correction procedures for different sensors that estimate the contributing factors from the atmosphere and correct for these factors.

2.2 Optical/Thermal Surface Properties

With the basics of EM energy and its interaction with atmosphere are covered. We need to know how to identify given surface elements by its different reflective or emissive properties.

2.2.1 Optical - Reflective properties

In this thesis we will refer to "optical" as the portion of the EM spectrum with wavelengths from 250 nm (Ultra Violet (UV)) to 2500 nm (SWIR). This includes the VIS, NIR and SWIR ranges in the EM spectrum. As seen in figure 2.2, the UV portion of the spectrum is almost fully absorbed by the atmosphere due to stratospheric ozone (O_3). By "optical properties", we refer to the parameters to describe reflection, absorption and transmission of incident solar radiation upon a surface . These properties depends on the nature of the surface, the wavelength of the incident EM energy and angle of illumination. As we're working with RS instruments that measure the reflected brightness of the surface, the reflective properties is the focus. Following the conventions from (Perovich, 1996), we can define some optical properties relevant to our case.
The spectral radiance $I(\theta, \phi, \lambda)$ is the power carried by an EM wave in a particular direction per unit area per unit solid angle. The spectral radiance is dependent on the zenith angle (θ) of incident radiation, where 0 is downwards and π is upward, the azimuth angle (ϕ) and the wavelength (λ). The spectral irradiance, $F(\lambda)$, is the spectral radiance projected onto a plane surface integrated over a hemisphere. Albedo (A), is the most used optical property for studies about sea ice (Perovich, 1996), and is defined as the fraction of incident irradiance that is reflected, or more formally

$$A(\lambda) = \frac{F_u(\lambda)}{F_d(\lambda)} \tag{2.3}$$

where,

$$F_d(\lambda) = \int_{\phi=0}^{2\pi} \int_{\theta=0}^{\frac{\pi}{2}} I(\theta, \phi, \lambda) \cos\theta \sin\theta d\theta d\phi \tag{2.4}$$

$$F_u(\lambda) = \int_{\phi=0}^{2\pi} \int_{\theta=\frac{\pi}{2}}^{\pi} I(\theta, \phi, \lambda) \cos\theta \sin\theta d\theta d\phi \tag{2.5}$$

$F_d(\lambda)$ and $F_u(\lambda)$ expresses the downwelling irradiance, radiance integrated over downward direction, and the upwelling irradiance, radiance integrated over upward direction. Albedo is a quantity of reflected radiance in all directions, but RS instruments measure the directional reflected radiance, so there's another important property called reflectance, or directional reflectance (ρ). Reflectance is defined as the same albedo fraction, but for a single incidence angle, it's a unit less quantity. Reflectance is what we used to identify different surface elements, by looking at its *reflectance curve*, more commonly known as spectral signature. A surface's reflectance curve is its reflectance over a range of wavelengths. Detailed knowledge about an objects spectral signature can allow us to identify these objects by its unique distribution of reflected radiation.

In RS terms, it's important to differentiate between Top Of Atmosphere (TOA) reflectance and Bottom Of Atmosphere (BOA) reflectance. Where TOA reflectances are values that includes atmospheric contributions and BOA reflectances are the surface reflectance with the atmospheric contributions removed. As other properties include fraction of transmitted radiance and fraction of absorbed radiance, a RS instrument only observing the reflected radiance in the optical range can not know how much of the incident irradiance is absorbed or transmitted. In our case we are constrained to only the reflectance of the surface.

2.2.2 Thermal - Emissive properties

As opposed to measuring radiation reflected of a surface, thermal RS measures the radiation emitted from the surface. The SIT product from NR is based on passive thermal remote sensing. Therefore it's important to know what exactly we are measuring in thermal RS.

All objects emit some EM radiation if its temperature is above 0 Kelvins (K). The radiation is described by Plank's radiation law. It describes radiation that occurs at all wavelengths, and radiation peaks at the wavelength that is inversely proportional to the temperature. For most natural bodies and surfaces on Earth, the peak thermal emission occurs in the IR region, while high-temperature bodies like the sun have a peak emission in the VIS and UV region. Formally we can write Plank's law as:

$$S(\lambda, T) = \frac{2\pi hc^2}{\lambda^5} \frac{1}{\exp^{\frac{ch}{\lambda kT}} - 1} \tag{2.6}$$

Where,

- $S(\lambda, T)$ is the radiant emittance in Watts per unit area per unit wavelength ($\frac{W}{m^3}$)
- T is the absolute temperature of the radiator in K
- h is the Planck's constant, $6.626 \cdot 10^{-34} Wsec^2$
- k is the Boltzmann's constant, $1.38 \cdot 10^{-23} Wsec/K$

Equation 2.6 describes the spectral distribution of the radiation emitted from a *blackbody*, also called blackbody radiation. A blackbody is a theoretical body that is a "perfect" absorber or "perfect" emitter, meaning that it absorbs all radiation, reflecting or transmitting none, and re-emits all over all wavelengths. A representation of a typical blackbody graph is shown in figure 2.3. Integrating the distribution over all wavelengths gives us Stefan Boltzmann's law:

$$S = \int_0^\infty S(\lambda, T) d\lambda = \sigma T^4 \tag{2.7}$$

where $\sigma = 5.669 \cdot 10^{-8} W/m^3 K^4$, giving us the total flux emitted by a blackbody. Differentiating the distribution with respect to wavelengths gives us Wien's law:

$$\lambda_m = \frac{a}{T} \tag{2.8}$$

where $a = 2898 \mu m K$. This gives us the wavelength at which the max emittance occur. Blackbodies are 100% efficient at transforming heat energy into EM energy, this is not the case for natural bodies, that have lower efficiency. This efficiency can be expressed as the ratio of the radiant emittance of a natural body to the radiant emittance of a blackbody at the same temperature:

$$\epsilon(\lambda) = \frac{S'(\lambda, T)}{S(\lambda, T)} \tag{2.9}$$

We call this efficiency factor, $\epsilon(\lambda)$, the spectral emissivity. There are three types of sources defined by how its emissivity varies over wavelengths:

- Blackbody: $\epsilon(\lambda) = \epsilon = 1$
- Graybody: $\epsilon(\lambda) = \epsilon < 1$
- Selective Radiator: $\epsilon(\lambda)$ varies with wavelength.

Most natural bodies are selective radiators, making it more difficult estimating thermal surface properties from the thermal radiation. Emissivity is also a

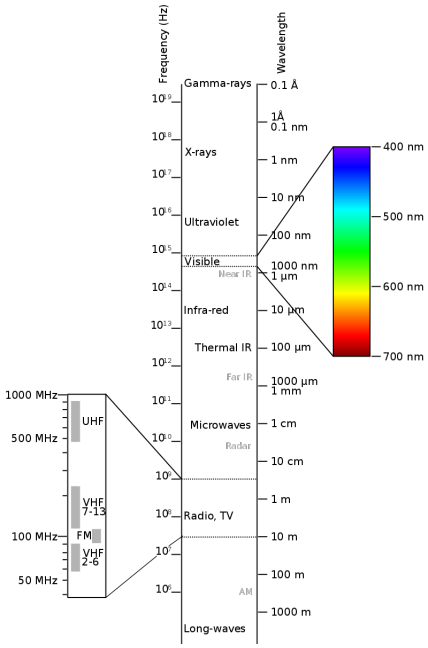

Figure 2.1: Electromagnetic Spectrum. Blacus - Own work based on: Electromagnetic-Spectrum.png, CC BY-SA 3.0, `https://commons.wikimedia.org/w/index.php?curid=22428451`

function of direction of emission. Directional emissivity is the emissivity at an angle relative to the normal of the surface. For most surfaces this can be denoted as the emissivity as a function of wavelength and angle relative to surface normal, $\epsilon(\lambda, \theta)$. For a thick medium, emissivity, ϵ is equal to the absorptance (α) of radiation, fraction of transmitted radiation through the surface of the medium, and can be related to the reflectivity (ρ) by

$$\epsilon = \alpha = 1 - \rho \tag{2.10}$$

. The reflectivity is also known as the surface albedo, closely related to the reflectance mentioned in previous section. Most surfaces follows this condition, and emissivity of a surface can be estimated by looking at the reflectance of surface in question. Not all surfaces necessarily agree to equation 2.10. Thin sea ice is not a thick medium, and radiation can be transmitted through the layer of ice and absorbed by the ocean water beneath, chapter 3 will explain this more thoroughly. With the equations above, knowledge about a particular surface's emissivity and the thermal radiation measurements, many important properties of the surface can be extracted, for example, Land Surface Temperature (LST), Sea Surface Temperature (SST), thermal inertia, soil moisture etc.

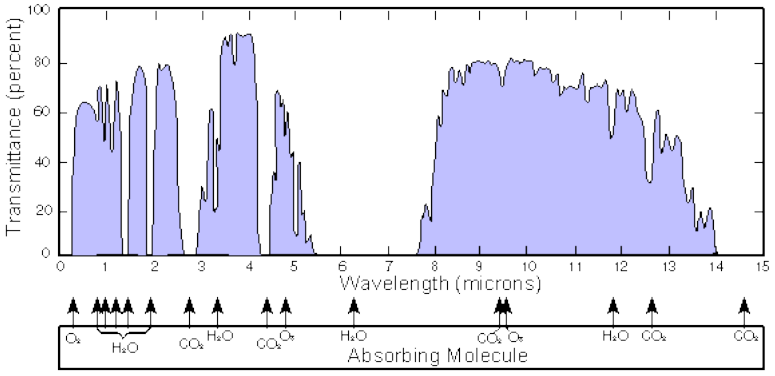

Figure 2.2: Atmospheric transmission windows in the infrared portion of Earth's atmosphere in wavelengths from 0 to 15 μm. From (Commons, 2017).

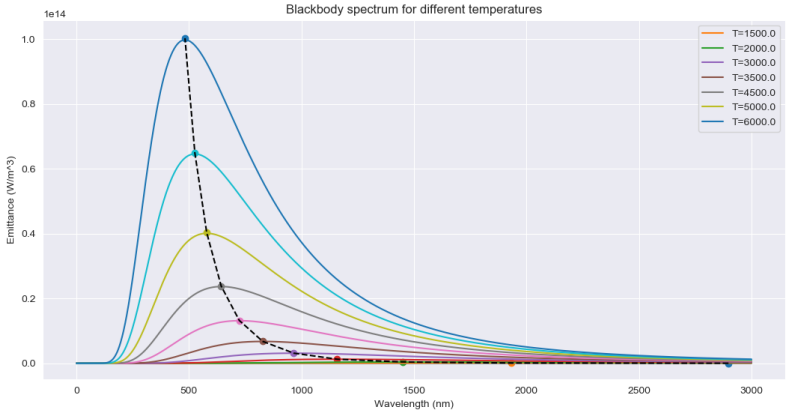

Figure 2.3: Representation of the blackbody radiation graph showing radiant emittance as a function of the wavelength given different temperatures ranging from 6000 K to 1000 K.

3

Sea Ice and the Thin Ice Thickness Model

This chapter explains the most important theoretical basis' for this thesis. The next two sections are based on the articles (Grenfell, 1983; Perovich, 1996) and (Yu and Rothrock, 1996).

3.1 Optical Properties of Sea Ice

This section will summarize the theory and difficulties by determining the albedo of sea ice, from the monograph, "Optical Properties of Sea Ice" (Perovich, 1996), with specific attention to the relation between SIT and the optical properties. Equation 2.3 shows us that the albedo must lie between 0, if none of the incident radiation is reflected, and 1, if all of the incident radiation is reflected. Figure 3.1a is a sub-scene of a S-2 scene covering layers of a high variety of sea ice on the south/east coast of Svalbard in the Barents sea, during march 15, 2019, before the melt season. The high variability is expressed in the TOA reflectance curves for the different sea ice surfaces (see figure 3.1b). Where open water has low reflective properties and thick/snow-covered sea ice has higher reflective properties. This can also be shown for the total albedo, albedo integrated over all wavelengths, where the surface total albedo is around 0.05 for open water, 0.5 to 0.7 for bare ice and 0.75 to 0.85 for snow covered ice (Perovich, 1996), figure 3.2 illustrates observed albedos for different ice types. As figure 3.1a is before the melt season, the sea ice surface conditions variability

will increase during the melt season as the sea ice cover evolves from highly reflective snow-covered sea ice to a darker combination of bare ice, melt ponds and leads (Perovich et al., 1998).

With all this in mind, to understand the variability in the total albedo and/or reflectance curves, a sound knowledge of the physical state and the complexities of sea ice and its structure is needed. Following the outline from (Perovich, 1996), the incident radiation on sea ice consists of both diffuse component from atmosphere and clouds, and direct radiation component from the sun, the contribution from each of the radiation components depends on the conditions. Some of the incident radiation is specularly/diffusively reflected from the surface, transmitted through the sea ice or absorbed in the sea ice. The relative sizes of each process is dependent on the physical properties of the sea ice, being the sea ice type, surface anisotropy, ice thickness, ice brine volume and impurities. We are interested in how the sea ice thickness relate to the spectral albedo or spectral reflectance of the sea ice. Some knowledge about the radiative transfer in the sea ice medium is important to understand how the spectral albedo behaves with variant sea ice structures. We know from equation 2.10 that the surface albedo is related to the absorption in the medium. Absorption in sea ice is defined by the absorption coefficients[1] for the primary components of sea ice: ice, brine and air. Absorption coefficients for sea ice can be determined by physical quantities and values of ice and brine absorption coefficients, where absorption in the air inclusions are assumed to be negligible, following the equation from (Perovich, 1996),

$$k_{si} = v_i k_i + v_b k_b \tag{3.1}$$

where v_i, v_b are the volume fraction of ice and brine, and k_i, k_b are the absorption coefficients of ice and brine respectively. Absorption for pure, bubble free ice is similar in magnitude and spectral shape to clean arctic sea water (Perovich, 1996). Minimum absorption happens in the blue of the VIS range and increases rapidly for longer wavelengths. The intricate structure of sea ice consists of ice crystals with inclusions of brine[2] and air, and sometimes solid salt, more common in newly formed ice. The inclusions have different indices of refraction than the surrounding ice crystals, causing stronger scattering in the medium. The wavelength dependence of the real portion of the index of refraction for ice, brine and air is weak at optical wavelengths. Optical wavelengths are much shorter compared to the sizes of the inclusions in sea ice. Since the scatterers are much bigger than the wavelength and far apart, the scattering in sea ice can be assumed independent of wavelength in the optical

1. Absorption coefficient is a measure on how quickly radiant flux is lost due to absorption alone.
2. Small droplets of highly saline water that forms in pockets between ice crystals.

regime (Grenfell, 1983). We can make some remarks about the absorption and scattering of sea ice in the optical wavelength range:

- Absorption is highly dependent on wavelength.
- Scattering has a weak wavelength dependency.
- Strength of scattering increases with amount and size of the inclusions in sea ice.

The albedo in the optical range increases with thickness at all wavelengths (Perovich, 1996), as the sea ice grows thicker in the initial stages of growth, backscatter in the ice are added and albedo rises rapidly. The ice is said to be optically thick when increasing the thickness any further doesn't affect the albedo. This asymptotic relationship is dependent on the wavelengths of the incident radiation, at shorter wavelengths (VIS) the albedo increase is still evident at around 0.25m thickness, while at longer wavelengths (NIR to SWIR range) the albedo looks asymptotic in nature (Perovich, 1996), this is also directly related to increased absorption in the longer wavelengths. This is the case for bare sea ice, however, a significant amount of sea ice usually have snow cover. Snow albedos for dry compact snow are usually very high, around 0.9, and have a weak dependency on wavelength (Grenfell and Maykut, 1977), this is due to the high scattering coefficients in snow. Even a 0.1-m-thick layer of wind-packed arctic snow is enough to eliminate any contribution from sea ice layer below the snow surface (Perovich, 1996). Figure 3.3b showcases observed albedo curves from possible stages of sea ice, and figure 3.3a showcases laboratory grown sea ice spectral albedo for each thickness.

3.2 The Thin Ice Thickness Model

The previous section explored how the physical state of sea ice is expressed in its optical properties, including the SIT. This section will have a closer look on how thin SIT is estimated from measurement of surface temperature and albedo, given the model outlines in (Yu and Rothrock, 1996). Specifications of any potential changes or assumptions made was unfortunately not shared as the "Sentinel4ThinIce" project is still in development.
The model assumes that the ice is thin and a linear temperature profile in snow and the rapidly growing young ice. The equation for energy conservation at the top surface in the cold season is

$$F_r + F_l^{dn} - F_l^{up} + F_s + F_e + F_c = 0 \tag{3.2}$$

. The first term is the net solar shortwave radiation heat flux at the surface, given by:

$$F_r = (1 - i_0)(1 - \alpha_s)F_{SW} \tag{3.3}$$

where the incident shortwave heat flux, F_{SW}, is estimated in clear sky conditions (Shine and Henderson-Sellers, 1985)

$$F_{SW} = \frac{1368.0(\cos(\theta))^2}{1.2\cos(\theta) + (1 + \cos(\theta)) \cdot 10^{-2}e_0 + 0.046} \tag{3.4}$$

where θ is the solar zenith angle, e_0 is the pressure of water vapour at surface. i_0 and α_0 is the transmittance of the ice/snow bulk and the albedo of the ice/snow surface respectively, and are both taken as a function of the snow and ice thickness, as we know from section 3.1. At night, equation 3.3 will be zero due to no incident solar radiation. The second and third term in equation 3.2 is the upward and downward longwave heat fluxes respectively.

$$F_l^{up} = \epsilon_s \sigma T_s^4 \tag{3.5}$$

$$F_l^{dn} = \epsilon_a \sigma T_a^4 \tag{3.6}$$

Where $\epsilon_s = 0.97$ and ϵ_a are the emissivities for the ice/snow surface and atmosphere, ϵ_a depends almost entirely on surface vapour pressure under clear sky conditions (Staley and Jurica, 1972). T_s and T_a are the temperature for the ice/snow surface and air temperature 2 meters above surface and σ is the Boltzmann Law Constant. The turbulent, F_s, and latent, F_e, heat fluxes are estimated by

$$F_s = \rho_a c_p C_s u(T_a - T_s) \tag{3.7}$$

$$F_e = \rho_a L C_e u(e_a - e_{s_0}) \tag{3.8}$$

where ρ_a is the air density, c_p is the specific heat of air, L is the latent heat of vaporization and C_s, C_e are the bulk transfer coefficients for heat transfer and water vapour. e_{s_0} is the saturation vapour pressure[3] at the surface. u is the surface wind speed at 2m above surface. With the assumption of linear temperature gradients in the snow and sea ice (Yu and Rothrock, 1996), the expression for the conductive heat flux, F_c, is given by

$$F_c = \frac{k_i k_s (T_f - T_s)}{k_s H + k_i h} \tag{3.9}$$

where k_i and k_s are the thermal conductivity of ice and snow respectively. T_f is the freezing temperature of sea water, and is derived from the salinity of sea water (Yu and Rothrock, 1996), $T_f = -0.055S_w$, where the sea water

3. Saturation vapour pressure is the pressure of vapour when it is in equilibrium with the liquid phase, solely increasing dependency on the temperature.

salinity S_w is measured in parts per thousand (ppt) and estimated from prior measurements. H and h are the thickness of sea ice and snow respectively. The snow layer, in similar fashion as in the optical domain, causes problems for estimating any properties of the sea ice. Snow cover not only increases the albedo considerably, but also reduces the thermal conductivity and elevates the thermal emissivity slightly (Yu and Rothrock, 1996). An empirical relationship between snow layer thickness and sea ice thickness derived by Doronin (1971) is applied:

$$\begin{aligned} h &= 0 && \text{for } H < 5\text{cm} \\ h &= 0.05H && \text{for } 5\text{cm} \leq H \leq 20\text{cm} \\ h &= 0.1H && \text{for } H > 20\text{cm} \end{aligned} \tag{3.10}$$

. The conductivity of snow, k_s is taken as 0.31 and the conductivity of sea ice, k_i, is estimated as from a relationship with the conductivity of pure ice k_0, the sea ice salinity S and the internal temperature of the ice slab T_i.

$$k_i = k_0 + \frac{\beta S}{T_i - 273} \tag{3.11}$$

where $\beta = 0.13 W m^{-2} kg^{-1}$, $k_0 = 2.034 W m^{-1} K^{-1}$. The internal temperature of sea ice is assumed to be equal to the surface temperature. The sea ice salinity is derived from an empirical relation with the ice thickness (Cox and Weeks, 1974),

$$\begin{aligned} S &= 14.24 + 19.39H && \text{for } H \leq 0.4m \\ S &= 7.88 + 1.59H && \text{for } H > 0.4m \end{aligned} \tag{3.12}$$

Equations 3.2 through 3.12 is refer to as the *thin ice thickness model*. Substituting (3.3) through (3.12) into (3.2) and solve for H will provide the estimate for sea ice thickness. Important to note that the measured parameter is T_s, the surface temperature from the SLSTR instrument stationed on S-3 satellite, and the sea ice thickness is estimated for every sea ice pixel in the scene.

3.3 Challenges

Snow cover is a huge obstacle in both observations in the albedo and thermal domain. This will increase the uncertainty of estimation of thin SIT considerably, and using an empirical model may alleviate the problem, but is not an optimal solution. Spectral albedo of snow is dependent on its grain size, snow-layer thickness and density. Measured snow albedos are generally high in the VIS and NIR, and drops off steeply between 800 and 1500 nm (Wiscombe and Warren, 1980). As most sea ice surfaces are covered with a layer of snow with its own spatial variability, we would expect to see spectral signatures related to the snow layer and if we follow the snow/sea ice relationship in equation

3.10 for thin SIT below 30 cm, we can assume the thickest layer of snow would be around 3 cm thick. Meaning that the spectral contribution from the sea ice below the layer of snow still contributes to the observed spectral albedo.

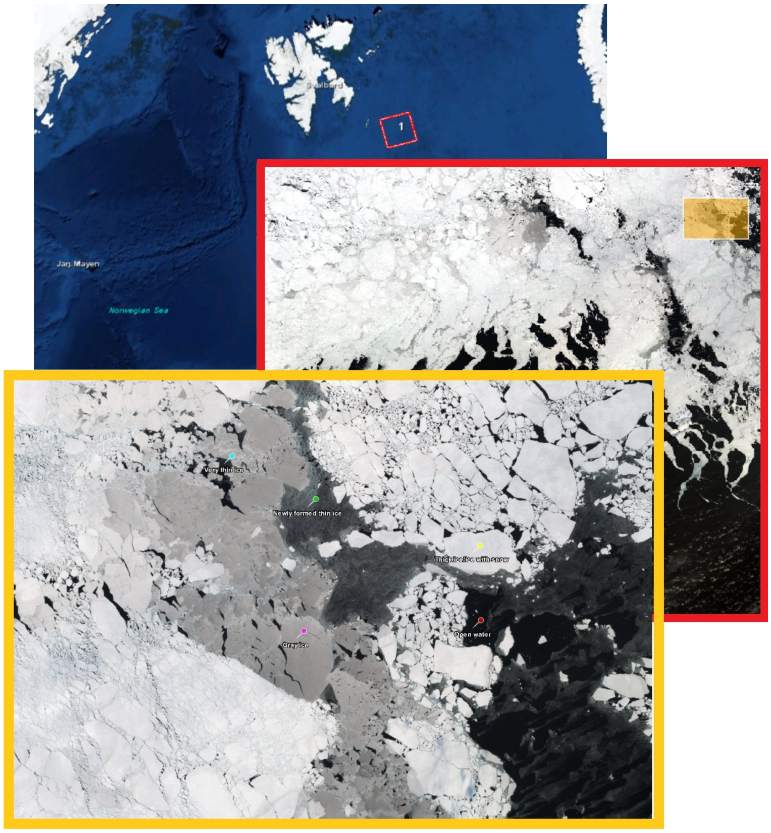

(a) S-2 subscene consisting of a highly variable sea ice surface. Scene is located south-east of Svalbard in the Barents sea, image was acquired on the 15th of March, 2019. Processed in Snap software from ESA.

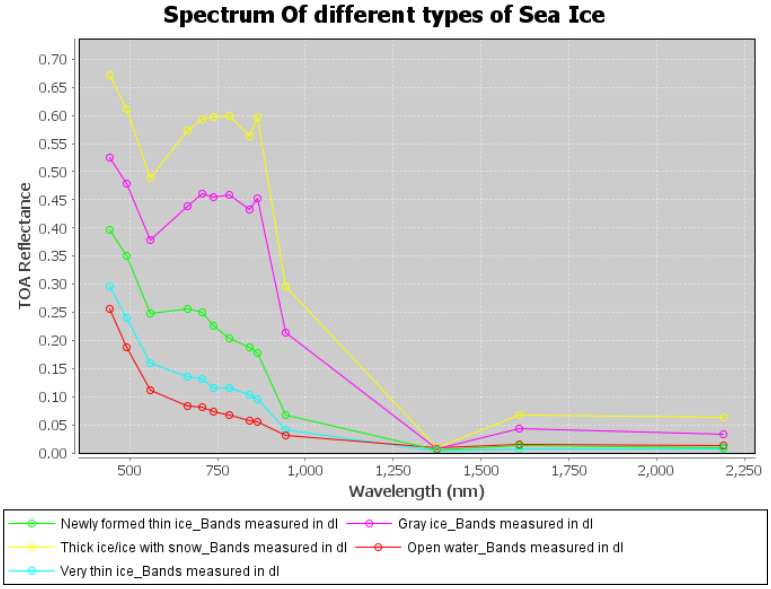

(b) Reflectance spectra from the S-2 bands, representing the different types of ice surfaces, displayed in figure 3.1a as coloured pins.

Figure 3.1: Area, scene, subscene and reflectance spectra of a different sea ice types, acquired by S-2.

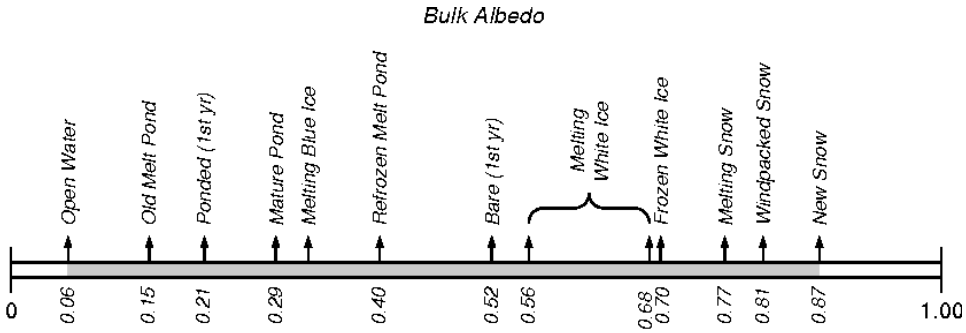

Figure 3.2: Range of observed values of total albedo for different sea ice types, from Perovich, 1996, p. 3, with permission from author.

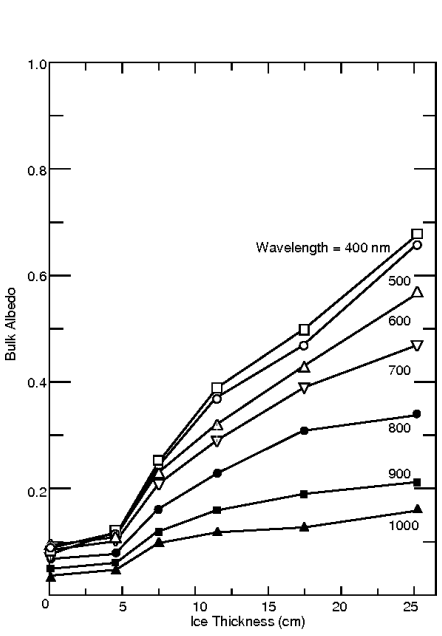

(a) Laboratory observations of increase in spectral albedo for thickening sea ice.

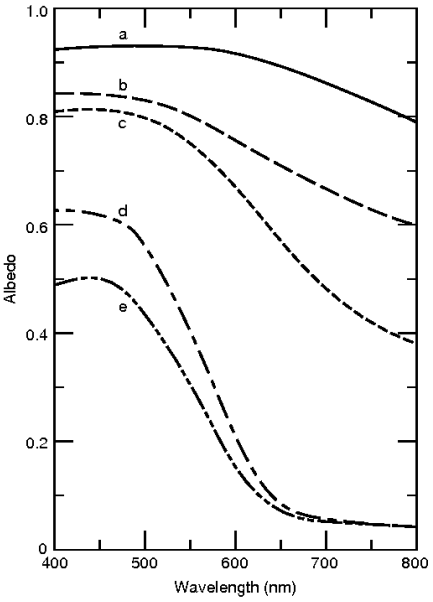

(b) Spectral albedos for different types of sea ice. a) snow-covered ice, b) cold bare ice, c) melting bare ice, d) early-season melt-pond and e) mature melt pond.

Figure 3.3: Spectral albedo graphs representing the spectral albedo variations in cases of changes in physical structure, being a) SIT and b) different evolutionary sequences of sea ice surfaces. Figure a) from Perovich, 1996, p. 8 and b) from Perovich, 1996, p. 9, with permission from author.

4

Satellite and Sensors

Two satellites are involved in this thesis. Sentinel-2 (S-2) and Sentinel-3 (S-3), both satellites are a part of ESA's Copernicus platform, focused on accurate, timely, and easy accessible Earth Observation (EO) information to improve the understanding of Earth's environment and mitigate the effects of climate change and ensure civil security. Each Sentinel satellite delivers an unique set of observations. We relate S-2 data, high resolution optical images, to thin SIT data derived from SST measurements from S-3. Because we are actively working with S-2 data, a more detailed description of S-2's Multi-Spectral Instrument (MSI) sensor and its data products is provided, while a more general description of S-3 and its sensor, SLSTR, is sufficient for our application.

4.1 Sentinel-2

The S-2 satellite is a wide-swath, high resolution, multi-spectral imaging mission, designed to monitor vegetation, soil and water cover, as well as inland waterways and coastal areas. The mission consists of two twin satellites, S-2A and S-2B launched in 2015 and 2017.

4.1.1 MultiSpectral Instrument (MSI)

Both satellites are equipped with the MSI imager, that provides 13 spectral bands covering the VIS, NIR and SWIR spectral regions ($400 - 2400nm$). MSI is a passive instrument that measures Earth's reflected radiance in the 13 spectral bands, represented in table 4.1 with the central wavelength, bandwidth

and spatial resolution for each S-2 band. The Spectral Response Functions (SRF) with the TOA (extra-terrestrial) solar irradiance spectrum is presented in figure 4.1. The MSI imager uses a push broom concept that works by collecting rows of image data across the orbital swath and utilizes the forward motion of the satellite. Radiation reflected from Earth and its atmosphere is collected by a three-mirror telescope and focused onto two focal plane assemblies, one for the ten bands in the VIS and NIR range and the other for the SWIR range.

4.1.2 S-2 MSI product specification

The available user products that S-2 provides are the TOA, level-1C, and BOA, level-2A, reflectances in cartographic geometry. Level-2A products are systematically performed at ground segment over Europe, but users can generate level-2A products through the Sen2Cor processor (Richter et al., 2018). Later sections will explain how level-2A product is not suitable for our application in the Arctic. Therefore we will focus on the specifics of the S-2 level-1C product.

S-2 level-1C products are a compilation of granules of fixed size, also called tiles. The tiles are arranged in 100 by 100 km images in UTM/WGS84 projection. The spatial resolution is the surface area measured on the ground and represented by an individual pixel, and varies from 10 to 60 meters dependent on a particular spectral band (see table 4.1). The temporal resolution is the time between image acquisitions of a particular point on Earth. S-2's revisit time depends on the coverage and mission objectives, but for the equator it will be 5 days in cloud free conditions. Closer to the poles, the revisit frequency will be higher due to more overlap between adjacent orbit paths. Areas that have less usefulness regarding S-2's main applications have a longer revisit time or no coverage at all, this mostly include open oceans. But S-2 do cover Arctic waters close to Svalbard and Greenland due to service requests from ESA's member nations or Copernicus. Radiometric resolution is the capacity of an instrument to distinguish differences in intensity. The greater the radiometric resolution, the greater the accuracy of the measurement. S-2's MSI imager have a radiometric resolution of 12 bits, enabling the instrument to sense $2^{12} = 4096$ potential levels of intensity values.

Level 1-C algorithm converts a numerical digital count (CN) of each pixel in the image (i, j) for each spectral band k to TOA reflectance. The conversion uses the equivalent extra-terrestrial solar spectrum, E_{sun}, the incoming solar angle, the zenith angle θ for each pixel in the image, and the absolute calibration, A_k, of the MSI imager. The conversion equation is (Gatti and Galoppo, 2018)

	S2A		S2B		
Band Number	Central wavelength (nm)	Bandwidth (nm)	Central wavelength (nm)	Bandwidth (nm)	Spatial resolution (m)
1	442.7	21	442.2	21	60
2	492.4	66	492.1	66	10
3	559.8	36	559.0	36	10
4	664.6	31	664.9	31	10
5	704.1	15	703.8	16	20
6	740.5	15	739.1	15	20
7	782.8	20	779.7	20	20
8	832.8	106	832.9	106	10
8a	864.7	21	864.0	22	20
9	945.1	20	943.2	21	60
10	1373.5	31	1376.9	30	60
11	1613.7	91	1610.4	94	20
12	2202.4	175	2185.7	185	20

Table 4.1: The spectral bands for the S-2 sensor (S2A and S2B), with the central wavelength, bandwidth and spatial resolution corresponding to each band. From Sentinel-2 MSI technical guide.

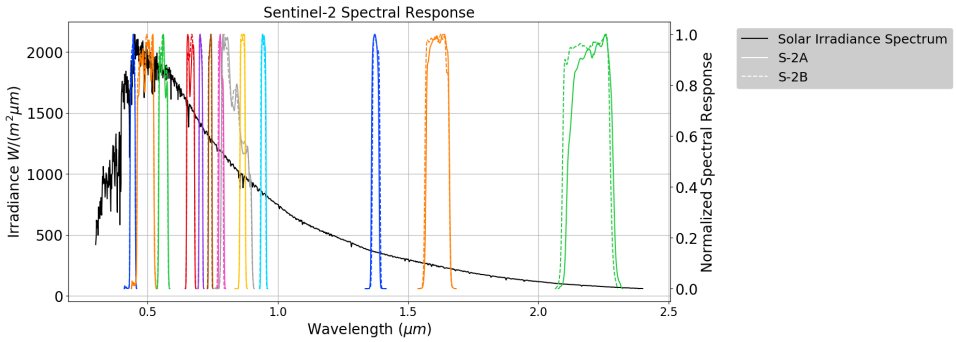

Figure 4.1: Zero air mass solar spectral irradiance in black solid line with the accompanying SRFs of S-2A in solid lines and S-2B in dashed lines. From American Society for Testing and Materials. Committee E21 on Space Simulation and Applications of Space Technology (2000) and ESA (2017).

$$\rho_k(i,j) = \frac{\pi \cdot CN_k(i,j)}{A_k \cdot E_{sun} \cdot d \cdot cos(\theta(i,j))} \tag{4.1}$$

where d is the correction for the Sun-Earth distance variation and utilises the inverse square law of radiation, that the intensity of radiation from a point source is inversely proportional to the square of the distance from the source. TOA reflectance values are within the range $\in (0, 1)$ and are converted to 16-bit digital number (DN) format. Users can retrieve the TOA values by dividing the DN values by the quantification value provided in the meta-data.

4.2 Sentinel-3

S-3 is a satellite mission developed for land, atmospheric, emergency security and cryospheric applications. The main objective being measuring sea surface topography, sea and land surface temperature and ocean and land surface colour. The satellite carries several instruments with its own applications, the two main instruments being SLSTR and Ocean and Land Colour Instrument (OLCI). The thin SIT data from MET is derived from SST measurements from the SLSTR instrument.

4.2.1 Sea and Land Surface Temperature Radiometer (SLSTR)

The main goal of SLSTR is to maintain continuity with the Advanced Along-Track Scanning Radiometer (AATSR) series of instruments on-board the now not operational ENVISAT satellite. The design incorporates the same basic functionality of AATSR with some new and advanced features including a wider swath, two channels dedicated to fire detection and higher resolution in some channels. SLSTR is a dual scan temperature radiometer, and provides global and regional SST and LST with a very high level of accuracy.

The SST is obtained via three calibrated IR channels at 3.74, 10.85 and 12μm. The SLSTR instrument and ground processing system are required to produce SST retrievals with an absolute accuracy of better than 0.3 K. SST measurements by the SLSTR instrument measures the temperature of the sea skin surface. The SLSTR products are generated separately in two instrument views and two resolutions, depending on optical channel. 500 meter resolution for solar reflectance bands and 1 km for thermal infrared bands.

5

Area of Interest and Data Preprocessing

Area of interest is the northern sea around Svalbard and Jan Mayen, north-western coast of Greenland and the Barents Sea where the sea ice information is much more valuable due to easier access for studies, in-situ measurements and frequent coverage from S-2.

5.1 Data Products

The SIT product received from MET is still in development, and unfortunately the technical specifics of the SIT retrieval algorithm and the uncertainty associated is not available. The theoretical background is based on the thin sea ice model outlined in section 3.2. The SIT product uses the SLSTR instrument on S-3 to determine surface temperature, and axillary data including air temperature measurements and 2-m wind velocity measurements. MET could only provide the algorithm image output product, but some specifics about the image product was given.

The data received from MET has a pixel resolution of 500 meters and coded with 8 bit unsigned integers where the values 100-130 corresponded to thin SIT from 0 cm to 30 cm. Other values included thick ice (90), cloud/no data (30), land (50) and open water (40). The goal is to find corresponding S-2 data that overlaps the SIT product at a reasonably close time differential, and making

sure the pixel location and information does represent the corresponding pixel location and information in the SIT product.

S-2 data acquisition/preprocessing was a difficult task because it required a lot of technical skill and many requirements for the data to be valid.

The preprocessing stage was done in several steps.

1. S-2 data aquisition by looking for overlapping products.
2. Choose valid S-2 products following some predefined requirements.
3. Apply atmospheric correction to get surface reflectance also called bottom of atmosphere (BOA) reflectance.
4. Co-locate and merge valid S-2 products for each thin SIT product received from MET.
5. Apply secondary cloud mask using S2Cloudless (Sinergise and Aleksandrov, 2018).
6. Take all the S-2 pixels corresponding to thin SIT pixels and begin analysis of correlation.

5.2 Overlap, Time Differential and Validity of the Data

Locating and finding overlapping S-2 scenes was done by extracting a geographical footprint and date time from the thin SIT product from MET and searching for Sentinel-2 scenes within the footprint and within an hour of the thin SIT raster. Sea ice can move fast if it's drift ice, meaning it's not attached or frozen to the shoreline (landfast ice). Drift ice is carried along by wind and sea currents, most notable being the Beaufort Gyre and the Transpolar Drift Stream in the Arctic region, as well as tidal motions. The resolution of the thin SIT product is 500 meter per pixel, because of this and the average down-sampling of the S-2 scenes down to the same resolution, the contribution from the smaller, fast moving ice floes are insignificant. With this, we can be confident that the co-located pixels correspond to the same sea ice. For insurance, the overlap is also validated qualitatively/visually.

We don't want to clutter our dataset with S-2 scenes that doesn't include any

valuable information, either being cloudy pixels, open water, land etc. The second step includes two more predefined criteria, the minimum percentage of thin SIT pixels within a S-2 scene and the minimum total of thin SIT pixels within a S-2 scene. The first criterion eliminates scenes that doesn't carry enough information to be considered valuable, and the second criterion eliminates scenes that have a high percentage of valid data, but an insignificant number of pixels. We count the valid pixels by creating two boolean masks, one being the valid thin SIT pixels (0-30 cm) and the second being the valid data footprint mask of the S-2 scenes reprojected onto the the same grid. The footprint mask is compared to the valid thin SIT mask, and we can count the valid pixels within the footprint and the percentage. The first criterion was set to 20% and the second to 2000 valid pixels.

5.3 Atmospheric Correction

Atmospheric Correction (AC) is the process of removing the effects of atmosphere on the observed reflectance values of remote sensing images. In our case we want the derive the surface reflectance or BOA reflectance from the TOA reflectance provided by the S-2 product. The importance of precise corrections for atmospheric propagation, topography and directional reflectance in the arctic is emphasized in (Malenovskỳ et al., 2012). Radiative transfer through Earth's atmosphere is heavily influenced by scattering processes like Rayleigh scattering and Mie scattering, as well as absorption processes due to aerosols and gases. In the Arctic, the challenges of AC may worsen due to low sun-zenith angles at beginning of summer and end of summer seasons, due to longer radiative paths through the atmosphere. A reliable thin SIT model needs to be consistent over time and area. Therefore the AC process needs to be consistent and of course reliable. S-2 provides calibrated TOA reflectances for each available wavelength, but atmospheric influence vary over time and area, this causes shifts in the distribution of the TOA reflectance values for different atmospheric conditions. Being differences in atmospheric properties like aerosol optical depth, solar radiation incidence angle, ozone concentration etc. As the specifics of the AC process is outside the scope of this paper, the decision of the AC processor was done based on the evaluation from (König et al., 2019). The chosen AC processor, ACOLITE (Vanhellemont and Ruddick, 2016, 2018), uses a dark spectrum fitting algorithm and had the closest resemblance to the in-situ spectra of the sea-ice floe surface compared to the other AC processors (ATCOR, iCOR and Sen2Cor) in the study. The study wasn't able to evaluate the AC quality in terms of absolute intensities, which may be a problem for the model, as the thin SIT model is dependent on the magnitude of the reflectance values, which is again dependent on absolute intensities. Therefore a part of the analysis and the decision on choice of thin SIT model will be dependent on the comparison between the TOA and BOA reflectances and it's correlation to

the thin SIT values.

Atmospheric correction is applied with default parameters with 60 meter resolution, as that's the lowest resolution the AC processor, ACOLITE, provides. Luckily, the processor can also merge several S-2 tiles before applying AC. Figures 5.2a and 5.2b illustrates the difference between the RGB composites of the TOA reflectances and atmospheric corrected BOA reflectances. The most clear distinction is the blue-ish haze, most likely caused by Rayleigh scattering, removed from the TOA reflectance values.

5.4 Co-Location, Merging and Cloud Masking

The final steps of the data preprocessing chain is to make sure that the S-2 reflectance pixel values correspond to the correct thin SIT measurements by resampling and co-locating the pixels. The thin SIT raster has resolution of 500 meter while the S-2 scenes have resolutions of 10, 20 or 60 meter resolution depending on the different bands. To make sure the information loss is kept at minimum during the resampling process, the average pixel value is calculated first before applying resampling. The drawback of this resampling method is that it creates mixed pixels, the average of the reflectances from several different surfaces, or in our case, several sea ice thicknesses. This method is better for maintaining information and averaging out noise. Co-location is done by mapping the pixels of the resampled S-2 rasters with an associated Coordinate Reference System (CRS) and transform to the pixels of the SIT raster with a different CRS and transform. This process is known as reprojecting. The S-2 TOA reflectance images are resampled, reprojected to the thin SIT raster's CRS and merged, while the already merged BOA reflectance images from the ACOLITE AC process are resampled and reprojected to the thin SIT raster's CRS. Figure 5.3 displays the output of the reprojected and merged S-2 rasters overlayed on top of the thin S-2 product.

5.4.1 Cloud Mask

The first cloud mask is provided by the thin SIT product, but a second cloud mask is applied to ensure that all of the cloudy pixels are not included in the analysis. Clouds can move fast within an hour and some pixels that may be marked as thin SIT, can be a cloud pixel in the S-2 image. The cloud mask provided by the thin SIT product is not optimal, meaning a second cloud mask filter will mask pixels that are falsely marked as thin SIT as cloudy pixels.

The choice of cloud mask was done based on previous work on the preceding

project task last semester. Where an extensive visual assessment was done to identify the best performing cloud mask for arctic regions. This assessment included scenes from S-2's MSI sensor and the NASA's Landsat-8 Thematic Mapper. The best performing, especially over sea ice, cloud mask was the S2Cloudless' pixel detector (Sinergise and Aleksandrov, 2018) provided by Sentinel Hub (Zupanc, 2017).

5.5 Implementation

This preprocessing chain is written and implemented in python using the high level Application Programming Interface (API) Rasterio from Mapbox (Gillies et al., 2013–). Rasterio is a Python raster data library, expressing GDAL's (GDAL/OGR contributors, 2018) data model, but with more idiomatic Python types and protocols, while performing as fast as GDAL's python bindings. The implementation of the steps 1-4 for the preprocessing stage is documented in the GitHub repository (Skogvold, 2019a).

Cloud masking was implemented using S2Cloudless python bindings (Sinergise and Aleksandrov, 2018). Because S2Cloudless doesn't include cloud shadow masking, the dilation parameter was set to 5 as an insurance for including the shadows in the masking. This assumes that incoming solar radiation isn't too close the horizon, which is not often the case in the Arctic.

5.6 Difficulties

As the poles on earth has the shortest revisit times for polar orbiting satellites, combined with the wide swath range of S-3, there's a wast amount of overlapping products within 1 hour. Because of the poor cloud masking from the thin SIT product, a lot of overlapping S-2 products had majority thin translucent cloud cover, making the information in the thin SIT product essentially useless. Despite the extent of overlaps, the amount of overlap that included thin SIT pixels was especially low for the 10 thin SIT products delivered. Of those 10, after visual examination, I was able to retrieve 3 thin SIT product that had clear skies in the optical and a wast amount of pixel information overlapping the thin SIT pixels. After all of the processing and qualitative assessment, the amount of S-2 pixels overlapping thin SIT pixels ended up on 500000. For most applications this is a good number of points for a regression analysis, but in RS applications, we need to capture as much variation in seasonal, atmospherical and yearly changes. But due to time constraints, the current information had to make due.

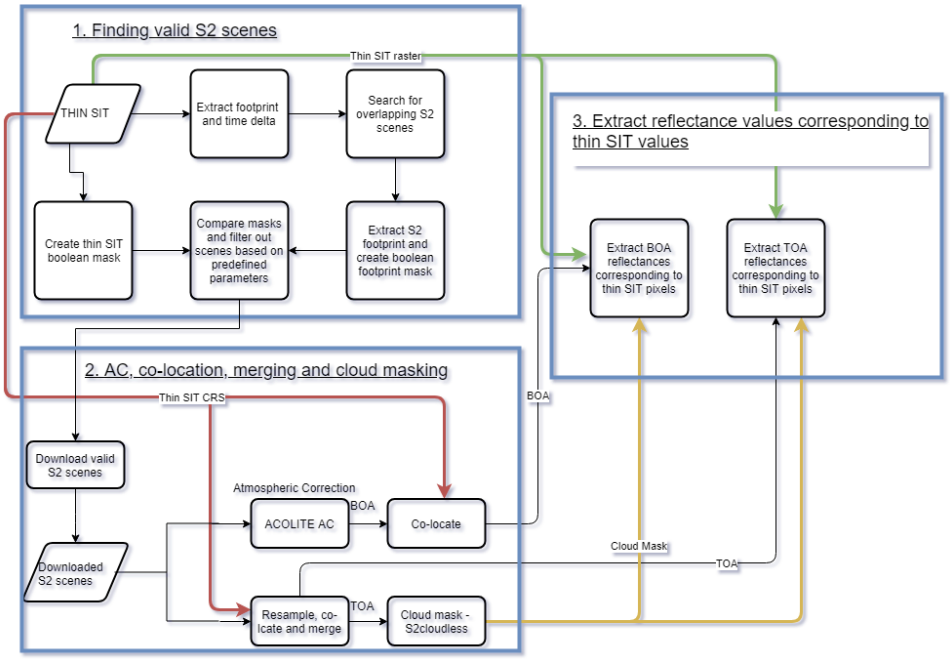

Figure 5.1: Data preprocessing chain as explained in Chapter 5, sections 5.2 through 5.4.

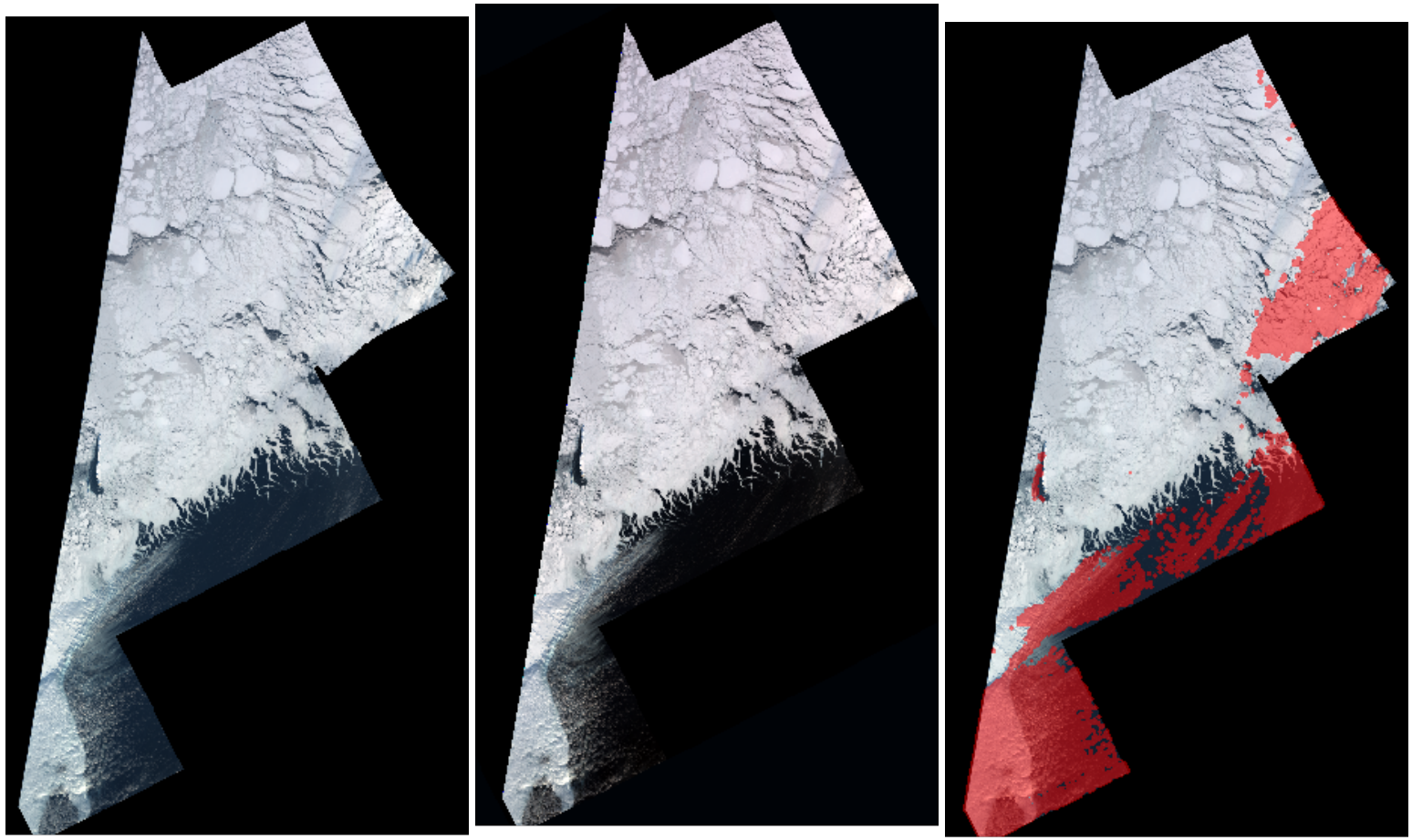

(a) RGB composition of the TOA reflectance values from the reprojected and merged S-2 scenes.

(b) RGB composition of the BOA reflectance values from the reprojected and merged atmospheric corrected S-2 scenes.

(c) Cloud mask applied to RGB composite of TOA reflectances

Figure 5.2: RGB composites of TOA (fig. 5.2a) and BOA (fig. 5.2b) reflectances, showing that the atmospheric component in TOA reflectance values are estimated and removed. Figure 5.2c shows the cloud mask overlay on figure 5.2a, the red cloud mask pixels will be removed.

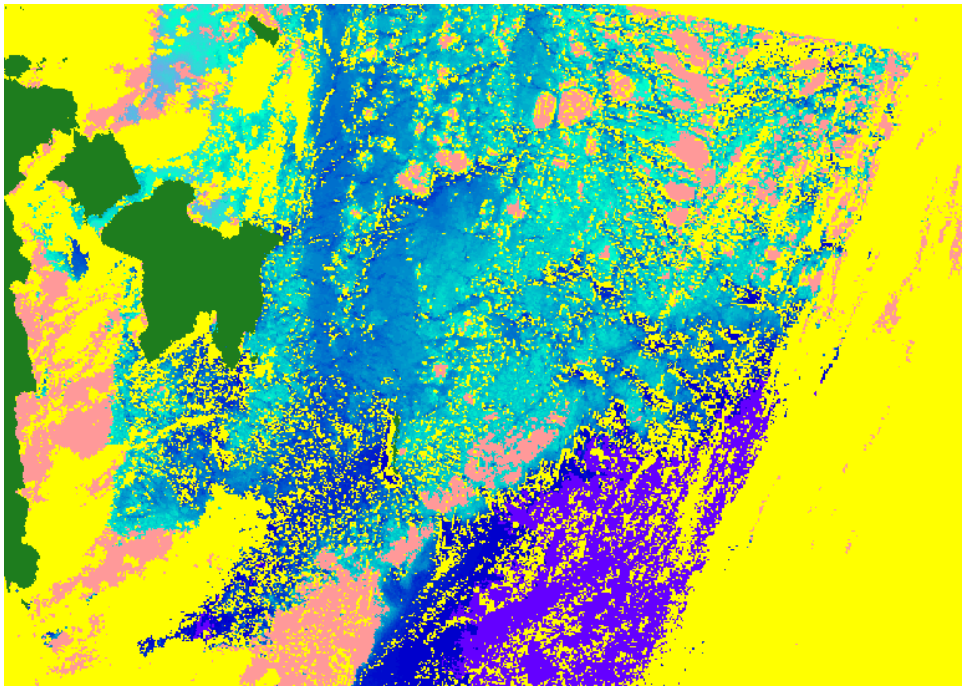

(a) Thin SIT product, the pixels are color-labeled. The blue gradients correspond to thin SIT values. Where dark-blue ⟶ cyan/light-blue are values from 0 cm to 30 cm at max.

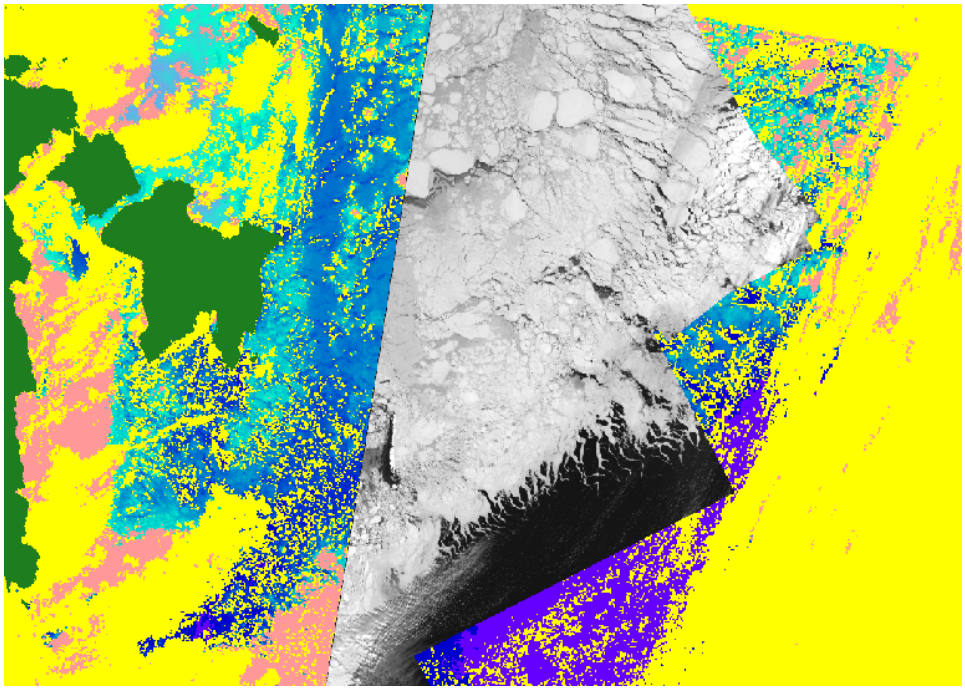

(b) Reprojected and merged S-2 level 1C band 4 (red ($\lambda = 665nm$)) raster on top of the thin SIT product.

Figure 5.3: Subset of final output of the reprojected and merged S-2 rasters on top of the thin SIT product and the thin SIT product. Location is the Barents sea, west of Svalbard.

6

Spectral Response of Thin SIT in Optical, DOS and Albedo Estimation

Before the actual regression implementation, it is wise to analyse the data and look for agreements with existing theory and explore potential outliers. After preprocessing, the available data was the TOA reflectance values and the BOA reflectance values. The best solution for a regression is often the simplest solution, and that includes the preprocessing, as the BOA reflectance retrieval is still inconsistent and not very reliable over arctic areas and adds a lot more complexity to the problem. Therefore finding a reliable regression using the TOA reflectance data directly from the S-2 level 1-C will be a preferred solution for most. Using only the TOA reflectances does introduce problems and complexities itself regarding reliability. This chapter will refer reflectance spectra as the mean or average reflectance spectra.

6.1 Top of Atmosphere

Because the thin SIT data is in discrete integers from 0 to 30 cm, we can analyse the spectra for each sea ice thickness level. The TOA spectral reflectance curve for each thickness in the thin SIT was estimated by taking mean value for each thickness in each band and plotting the reflectance curves together, represented in figure 6.1a. Each curve has a consistent shape, this is to be expected

as every pixel is sea ice surface. The increasing thickness relates to an increase in reflectance for every band. Figure 3.3a in chapter 3 represents an increasing spectral albedo with both the increasing SIT and shorter wavelength, we can see a similar behaviour in figure 6.2a. The slopes of the longer wavelengths in the SWIR region are more shallow than the shorter wavelengths in the VIS and NIR regions. Absorption of snow and sea ice increases with longer wavelengths resulting in a weaker reflectance, it doesn't take more than a few centimetres of sea ice to absorb most radiation beyond 1000nm (Perovich, 1996). This is quite clear for all thickness spectra in figure 6.1a, where the reflectance drops considerably after 800nm.

Atmospheric scattering mechanisms and adjacency effects are both components that attenuates and distort the true surface reflectance information. Adjacency effects is the scattering of light from neighbouring surfaces into the surface field creating a information overlay. Because of spatial mixture and high contrast of leads, open water, bright ice and snow surfaces, the impact of adjacency effects are believed to be large for S-2 imagery (König et al., 2019). Scattering effects due to Rayleigh scattering and Mie scattering as well as absorption due to aerosols and gas are also degrading factors and much more prominent in the shorter wavelength regions, VIS and NIR. The propagation through atmosphere causes an offset and gain to at-sensor radiance measurements (Richter and Schläpfer, 2013). The atmospheric attenuation of the observed TOA reflectance are clear when we compare the VIS region with known measured sea ice surface reflectance from literature (Perovich, 1996; Perovich et al., 1998), where surface reflectance from snow/sea ice surfaces are quite constant in the VIS range. We observe a drop from band 2 to 3 and an increase from band 3 to 4 (see figure 6.1a), this is also observed in (König et al., 2019). The atmospheric degradation becomes a huge problem for modelling surface properties like SIT due to changes in atmospheric conditions over time and geographical area. In our application of finding a regression model for thin SIT, reliability over temporal and spatial domain becomes an increasing concern when using TOA reflectance values.

As an attempt to estimate more reliable BOA reflectance values, we applied an AC processor to each S-2 image product (see section 5.3).

6.2 Bottom Of Atmosphere

The ideal case for BOA reflectance retrieval for optical RS is that the BOA spectral signature for a particular surface should match the same spectral signature as we were to measure the same surface at surface level. Section 5.3 mentioned the AC process and the difficulties for modelling atmospheric conditions in the

Arctic. The BOA reflectance spectra for each thickness is illustrated in figure 6.1b. The reflectance values across the VIS and NIR range are more aligned and better a representation of we would expect from the observed spectral albedo in literature (Perovich, 1996; Perovich et al., 1998) and the spectral albedo shapes in figure 3.3b. Band 9 and 10 are neglected by the selected AC processor, ACOLITE, due being primarily used for AC. Figure 6.2b illustrated the individual band reflectances as a function of thin SIT, the band reflectances in the VIS and NIR region are more aligned for both reflectance value and slope for each SIT level. The SWIR bands show the same relationship as in TOA reflectances, with a shallower slope.

We can qualitatively evaluate the validity of the BOA reflectance shapes by comparing with previously observed spectral albedos, but the reflectance magnitudes cannot be evaluated without knowledge about the true surface reflectance, usually from in-situ measurements. The magnitude of the reflectance values is important for when we want to gather reflectance information from several different scenes spread over time and space, as under- or over-corrections due to inaccurate atmospheric modelling can result in higher variance in surface reflectance values for similar surface types. Because the BOA reflectance spectra shapes are similar to previously observed surface reflectances, we can make a reasonable assumption that the spectral relationship between bands is more representable for the sea ice surface we're observing.

Next section will attempt to apply an easier and less complicated AC procedure, called Dark Object Subtraction (DOS), and see if that's a good enough approximation for the surface reflectance.

6.3 Dark Object Subtraction

DOS is a simple method designed to remove atmospheric scattering or "haze" from multispectral imagery and only requires information from the image data. DOS correction assumes a constant haze value throughout the entire scene, which is often not the case, but it does accomplish a first order correction. The assumption is based upon the high probability that there exists a few pixels that are black, meaning no reflectance from the surface is captured, due to vast amounts of pixels in each scene. These "dark objects" can be shadows due to topography and optically thick clouds, where the sensor shouldn't detect any radiance. However, due to atmospheric scattering effects, these "dark objects" will not be completely dark, the sensor captures a non-zero radiance that must be subtracted from the particular spectral band to remove the the atmospheric scattering. The simplest method for this is to find the minima pixel value for each band and subtract that minima from the rest of the scene. This was done

for each scene as an attempt to remove some of the additive atmospheric effects distorting the image. The simplicity of the method is attractive for usage in processing chains, where human intervention is not wanted.

Figure 6.1c represents the "haze" corrected spectral curves for each SIT. As previously mentioned in section 2.1.2 the shorter wavelengths scatter much more due to the nature of Rayleigh scattering, the subtracted amount for the three first bands are substantial compared to the following bands. The simplicity of the method also comes with some huge drawbacks. Secondary atmospheric scattering effects such as skylight is not considered, atmospheric absorption and adjacency effects are also not included. The values of the dark objects selected may not conform to a realistic relative atmospheric scattering model (Chavez Jr, 1988). The lack conformity can lead to an incorrect spectral relationship between the bands. The constant relationship usually seen in the VIS range for sea ice surface reflectance in literature is not represented in the spectral curves (figure 6.1c) and worsened compared to the non-corrected TOA reflectance curves (figure 6.1a).

Multi spectral RS images of scenes only including thin sea ice and water will realistically have no shadows due to topography and the dark pixels are likely water pixels. Dark waters are sometimes a good indicator for dark objects, but it depends on how sediment free the water is, if the water is not completely clear, it does not represent a valid dark object. Atmospheric radiance contribute around >85% of total signal in oceanic waters, >60% for sediment rich waters and >94% in very dark waters (König et al., 2019). The S-2 scenes used in this analysis includes water bodies close to coastlines of Svalbard archipelago, Severny Island, and Franz Josef Land, meaning the water includes redistributed sediments from rivers and rocks. The melting sea ice also increases the sediment levels (Kipp et al., 2018). The validity of the dark objects may be questioned and also the main cause to the seemingly over-corrected spectra.

The most affected band to this over-correction seems to be band 1 (442 nm) (see figures 6.1c and 6.2c). Compared to the ACOLITE processed BOA data and non-corrected TOA data, the shape is less consistent and more erratic. It's the shortest wavelength and sensitive to atmospheric scattering, the DOS corrections for each S-2 scene must have been inconsistent.

Band	ω_{b_i}
B01	0.128
B02	0.133
B03	0.127
B04	0.104
B05	0.096
B06	0.088
B07	0.080
B08	0.072
B8A	0.063
B09	0.057
B10	
B11	0.017
B12	0.005

Table 6.1: Distribution of weighting coefficients for estimating total albedo, band 10 is neglected due to being located in an atmospheric absorption window and designed for cirrus detection.

6.4 Estimated Total Albedo

From the previous sections, we can state that there's an obvious correlation between the spectral signature and thin SIT estimates. As the shapes of the spectral signatures and the relative reflectance increase to thin SIT is similar across the bands, we can combine the bands by estimating the total albedo. The total albedo is calculated as the integration of reflectance across the incident EM spectrum. Because we only have the reflectance information in some select wavelengths (see table 4.1), we can estimate the total albedo by a weighted sum using a similar procedure defined by Vanino et al. (2018),

$$A = \sum_{b_i} \rho_{b_i} \cdot \omega_{b_i} \tag{6.1}$$

where ρ_{b_i} is the reflectance in the i'th band, and w_{b_i} is the weighting coefficient representing the solar radiation fraction derived from the extraterrestrial solar irradiance spectrum within the spectral response curves of the i'th band. The weighting coefficients are calculated as.

$$\omega_{b_i} = \frac{Esun_i}{\int_{0.4}^{2.4} R_{s\lambda} d\lambda} \tag{6.2}$$

where $R_{s\lambda}$ is the extraterrestrial solar irradiance for wavelength λ and provided by (American Society for Testing and Materials. Committee E21 on Space

Simulation and Applications of Space Technology, 2000). $Esun_i$ is the mean solar exoatmospheric irradiance for the i'th band, and is retrieved by convolving the solar irradiance and relative spectral response over wavelengths,

$$Esun_i = \frac{\int SRF_i \cdot R_{s\lambda} d\lambda}{\int SRF_i d\lambda} \tag{6.3}$$

where SRF_i is the spectral response function for band i provided by (ESA, 2017) and illustrated with the solar irradiance spectrum in figure 4.1. The weights are normalized, such that $\sum_{b_i} \omega_{b_i} = 1$. The spectral response functions are almost identical for both S-2A and S-2B, we can assume the difference in the weight distribution is negligible. The total albedo is estimated for TOA reflectance, BOA reflectance and TOA reflectance with DOS applied. Table 6.1 are the weight values corresponding to each band, where the VIS and NIR dominates the albedo contribution and the SWIR bands are essentially neglected. Figure 6.3 illustrates the total albedo for TOA, BOA and TOA with DOS applied. The error bars represents the standard deviation for each thickness level and is quite consistent over the whole SIT range.

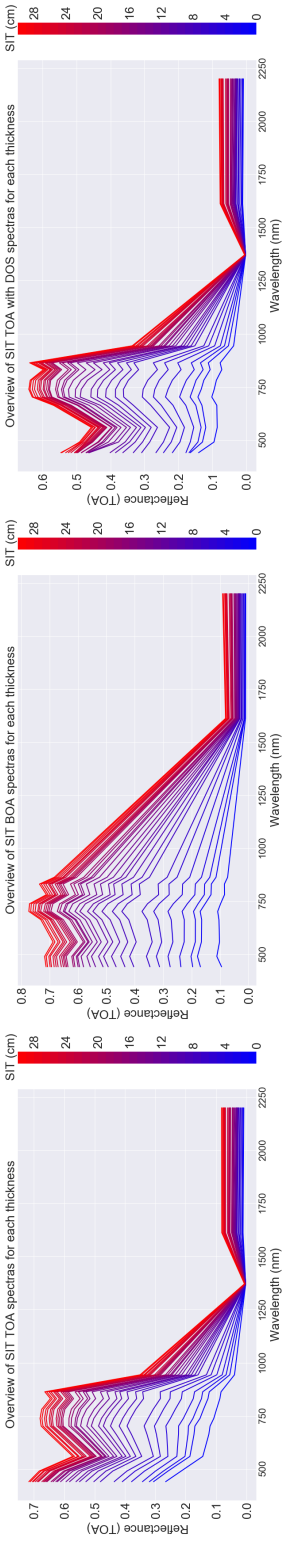

Figure 6.1: Spectral reflectance curves for each sea ice thickness level. a) TOA, b) BOA, c)TOA with DOS.

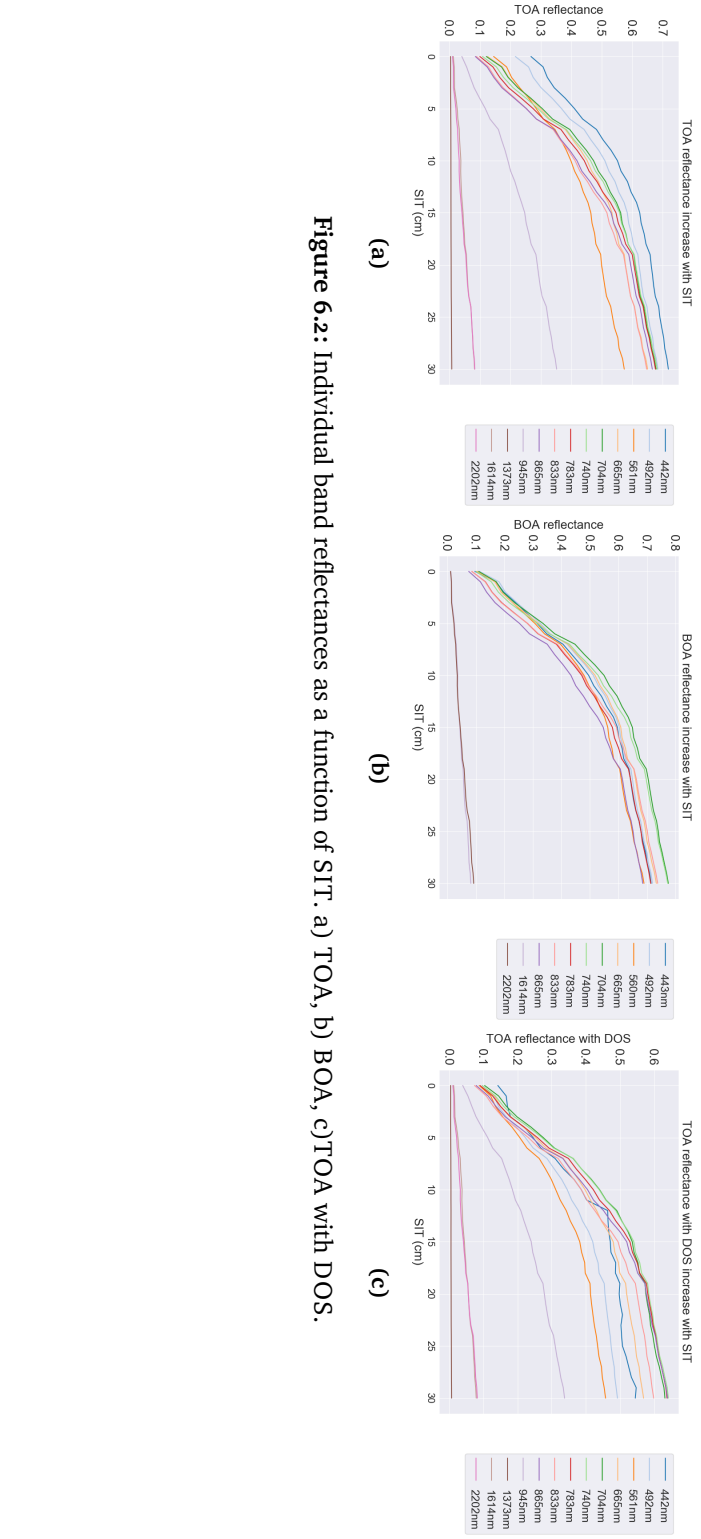

Figure 6.2: Individual band reflectances as a function of SIT. a) TOA, b) BOA, c)TOA with DOS.

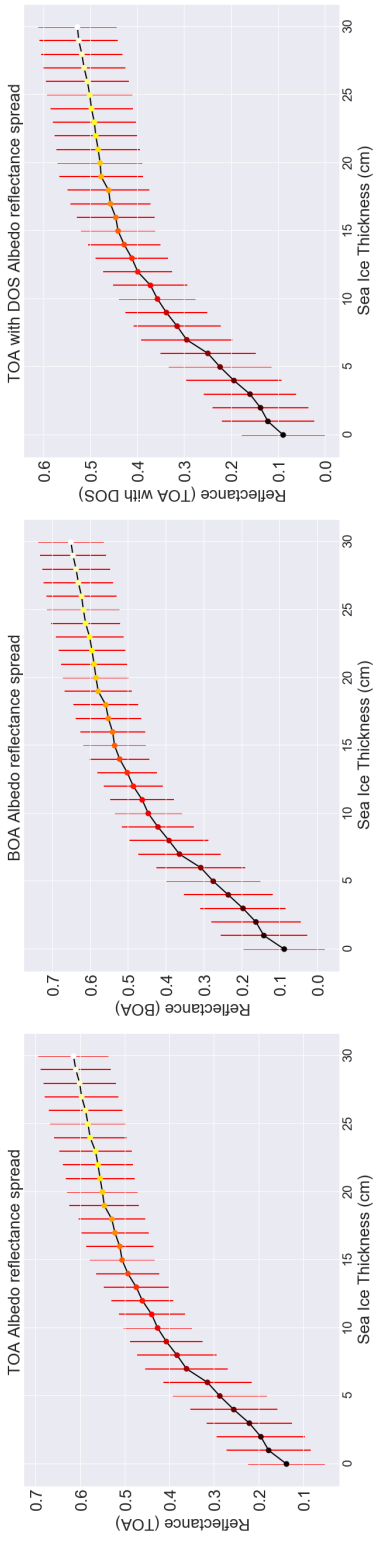

Figure 6.3: Total albedo estimates as a function of SIT. a) TOA, b) BOA, c)TOA with DOS.

/7

Thin SIT Regression Model

The previous chapter explored the spectral signatures of sea ice as a function of its thickness showing a clear increase in reflectance for thicker levels of sea ice, however the reflectance saturates as the thickness approaches 30 cm. We have also mentioned some advantages and disadvantages for different processing schemes, using TOA, BOA or TOA with DOS reflectances. This chapter will explain the methods used for finding a SIT estimate function with S-2 band reflectance as input using regression methods and present the results in light of the particular data-set and the its potential drawbacks. Chapter 6 presented the different data-sets to work with:

- Univariate, Combined bands using total albedo estimation:
  - TOA albedo.
  - TOA with DOS albedo.
  - BOA albedo.
- Multivariate, selected set of bands (band 10 is neglected for all).
  - TOA band reflectances. (band 10 neglected)
  - BOA band reflectances (band 9 and 10 neglected)

– TOA with DOS band reflectances (band 1 and 10 neglected)

For TOA,Band 10, or the cirrus band is neglected due to being specifically used for cirrus detection. For BOA, ACOLITE AC processor neglects band 10 and 9 due to being specifically used for atmospheric correction (Vanhellemont and Ruddick, 2016). For TOA with DOS, Band 1 is neglected due to reasons mentioned in section 6.3.

The first method would be a univariate regression using the band combined total albedo estimations. This is the simpler method we implemented, and gives a very rough, but efficient and easy to interpret results. The second and much more complex method aims to utilize all of the spectral information available to us. A multivariate machine learning method using gradient boosting technique, where each band is a feature. More detailed description of the specific methods and its implementation is presented below followed by the last processing step before applying regression, outlier detection.

7.1 Methods

7.1.1 Non-linear least squares

The general theory of the Non-Linear Least Squares (NLLS) optimization process is outlined in appendix A. The goal is fit a function of non-linear nature with a set of free parameters, by finding the optimal parameters for the data set. Figure 7.1 displays the thin SIT as a function of the TOA albedo estimate values, with the cyan coloured line representing the mean value for each level of thickness. We can clearly see that the thin SIT is increasing faster as the corresponding albedo values go towards 1. As we want to map the albedo values to an estimate of thin SIT, the model chosen needs to be of this nature. The models $f(x;\vec{\beta})$ chosen for evaluation on the thin SIT data-set where a logarithmic, three degree polynomial and power function defined as,

- Logarithmic:
$$f(x) = a - b\log(x \cdot c) \tag{7.1}$$

- Power:
$$f(x) = \left(\frac{x-a}{b}\right)^c + d \tag{7.2}$$

- Polynomial ($n = 3$):
$$f(x) = ax^3 + bx^2 + cx + d \tag{7.3}$$

Where x is the data and a, b, c, and d are the free parameters to optimize. The

optimization process was implemented using SciPy (Jones et al., 2001–), an open source scientific tools API for Python.

7.1.2 LightGBM, Gradient boosting machine

GBM is a widely used algorithm for machine learning purposes, due to its efficiency and accuracy. The general idea is to compute a sequence of simple trees, where each successive tree is built for the prediction residual errors of the preceding tree. Also called an ensemble model of decision trees. GBM selects a loss as the objective function and uses an additive model of the many weak learners (usually regression trees) to minimize the loss.

LightGBM (Ke et al., 2017) is a gradient boosting framework optimized for accuracy and training time distributed by Microsoft. The model uses a histogram based algorithm that discretizes continuous features to speed up training and decrease memory usage. It grows the trees leaf-wise, as oppose to level wise, to increase the loss reduction. LightGBM was chosen due to its ability to handle large data-sets extremely efficient, accuracy focused method and efficient training. LightGBM is prone to overfitting due to its "best first" leaf wise method. The parameters where chosen such that there's a good balance between accuracy and low chance of overfitting. Specific parameters tuning was chosen after some quick initial runs and following the recommendations from LightGBM's documentation:

- `min_data_in_leaf`: 1200, set high due to large data-set.
- `num_estimators`: 1500, number of trees in the model
- `max_bin`: 65, increase general power (reduce overfitting)
- L2 regularization, weight decay: 0.01

The objective function was set to sum of squared residuals, called regression L2 loss. The default value was used for the rest of the parameters. The training process was implemented using LightGBM python API (Microsoft, 2017).

7.2 Outlier Detection

Outlier detection is an important step to make sure the data doesn't include any unwanted clutter that may interfere with the regression fit by gravitating the regression process towards the outliers. We want to keep the one-to-one relationship between the actual reflectance information from the optical and the thin SIT information, some pixels may be not represent the thickness information. These pixels will be regarded as outliers in the data. These can

be edge pixels, pixels with close to zero values due to average resampling by including pixels outside the S-2 tiles, cloudy pixels that escaped the cloud masking and cloud shadows. Cloudy and cloud shadow pixels are hard to catch, because they can either come from thin translucent clouds or very bright clouds, and the shadows are naturally darker. Pixels from cloud shadow is especially prevalent when the sun zenith angle is high (sun being close to the horizon), and the cloud shadows cover a greater surface area visible to the sensor. Edge pixels are easy to catch as they are always close to zero independent of thin SIT.

The thin SIT data is in discrete numbers from 0 to 30 cm, therefore we can look at the individual distributions for each thickness level and determine the outliers by their deviation from the mean reflectance values of a specific SIT. We assume a Gaussian distribution for every thickness level and apply a simple standard deviation method to determine the cut-off for identifying outliers. The standard deviation from the mean in a Gaussian distributed data set can be used reliably to estimate the percentage of values in the set. We can define the cut-off as multiples of the standard deviation representing different ranges in the data. If we call this multiplier m, the cut-off is defined as,

$$T_{co} = m \cdot \sqrt{\sum_{i}^{N} \frac{(x_i - \overline{x})^2}{N-1}} = m \cdot \sigma \tag{7.4}$$

. The cut-off, T_{co}, is calculated for every thickness level and the values are kept if they follow the condition,

$$x_i \text{ is } \underline{\text{not}} \text{ an outlier if } |x_i - \overline{x}| < T_{co} \tag{7.5}$$

where m is chosen to be 2, covering 95% of the data set. Figure 7.1 displays the TOA albedo distribution before and after the outlier detection. This method is applied for every band/albedo estimate in every data set before applying regression analysis.

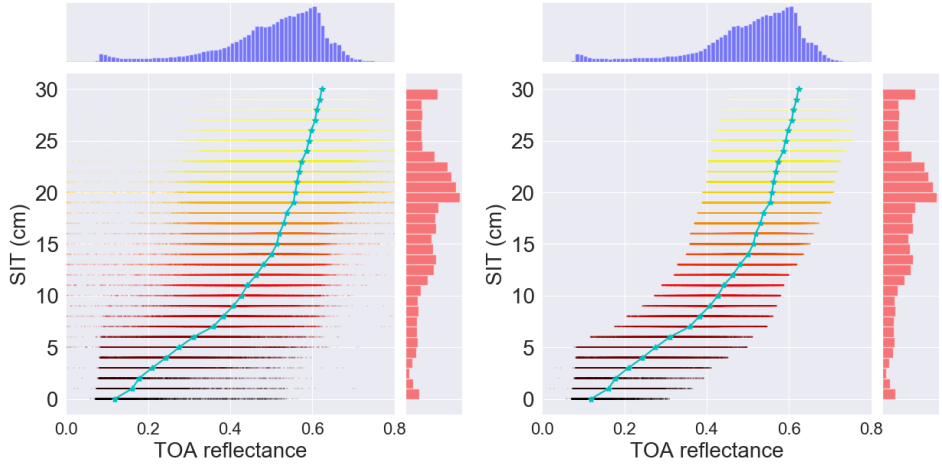

(a) Before outlier detection.

(b) After outlier detection.

Figure 7.1: Outlier detection, and distribution of data.

7.3 Results

There are effectively four regression models, three univariate models defined in section 7.1.1 using the total albedo estimates, and one multivariate model defined in section 7.1.2 using the different band reflectances. The metric used for evaluating "goodness of fit" is the RMSE defined as:

$$RMSE = \sqrt{\frac{\sum_i^N (\hat{y}_i - y_i)^2}{N}} \tag{7.6}$$

where $\hat{y}$ is the prediction, y is the observed value and N is total number of samples evaluated. RMSE is a quadratic scoring rule that also measures the average magnitude of the errors, also called residuals. RMSE is more sensitive to larger residuals due to calculation of squared residuals. Lower RMSE values correspond to a better fit. Because we take the root of the squared residual, the value is within the same range of the data set and easier to interpret. It's also a absolute measure of fit, meaning that as long as we have a prediction and observed values, the RMSE can easily be obtained. We sampled random smaller sub-sets of same size from each data-set and calculated the RMSE value from the predictions from each sub-set for each model fitted to appropriate data set and took the average of the RMSE values. The final average RMSE value for each model and data-set is presented in table 7.1.

	RMSE Values			
	Model/data	BOA	DOS	TOA
Band Reflectance	**LightGBM**	2.675	2.635	2.567
Total Albedo	**Poly**	5.390	6.180	5.290
	Log	5.174	5.897	5.103
	Power	5.012	5.867	4.956

Table 7.1: RMSE values for each data and model, calculated from random subset sampling and averaged.

7.3.1 Total albedo, univariate non-linear regression

Figure 7.1 illustrates the TOA total albedo data with it's mean line and distribution over albedo and SIT data. The albedo distribution reflects the overlap of albedo values making it harder to accurately predict SIT in those upper ranges, the mean line is the same as in figure 6.3a, but with flipped axis to better illustrate the goal of mapping from reflectance/albedo to SIT. The distribution of SIT on the y-axis represents the spread in the specific data set we have, and shows us that a big portion of the SIT data is located between 15 to 25 cm.

The increase in albedo starts to saturate towards thicker sea ice levels, and represents some kind of monotonically increasing function. The three functions chosen are represented with its free parameters in section 7.1.1 as well as the implementation. The were some initial problems in the implementation regarding the first fitted curves as they clearly didn't show a good fit. After some extensive testing with normalizing the SIT data to match the same range as the albedo data ($[0, 1]$), and choosing the initial parameters, the best solution was to fit the normalized SIT data to the albedo data and then apply the same parameters to the inverse of the fitted function. The issue seemed to stem from the SciPy implemented algorithm where it struggled with fast increasing data, but performed much better for saturating functions. The inverse of the polynomial function was too complicated to solve for hand. The easiest solution was to linearly interpolate the fitted polynomial such that the interpolation outputs the thin SIT estimate as a function of the albedo input. The results for each fitted function to each albedo data-set is represented visually in figure 7.2, the RMSE values for each fitted line is found in table 7.1.

Figure 7.2 illustrates the fitted functions for each data-set. All of the fitted lines look quite similar for each data-set, the best fit visually is the polynomial function as it follows the mean line best. The RMSE metric for the total albedo data-sets in table 7.1 was only evaluated for predicted SIT values between 0 and 30 cm, as we have no information about thicker sea ice. The RMSE metric

shows that the power function performs best for all data-sets, followed by the logarithmic function and surprisingly the worst performer was the polynomial fitted function.

TOA total albedo data gave us the best fit over all the fitted functions, coincidentally is also the least processed data set. TOA with DOS applied gave us the worst results over all data sets, and most likely due to the higher variance from inconsistent haze correction from the DOS process outlined in section 6.3. BOA total albedo data came in second place, as it's probably due to some under-corrections or over-corrections done by the AC processor, causing some slight changes between the scenes, again causing a slightly higher variance.

A big portion of the data-set is centred around 20 cm. Because the RMSE metric calculates the mean of all the squared residuals, the RMSE value will be more biased towards this range. To illustrate the performance of the fitted power function for each data-set we calculated the RMSE metric for specific intervals of thin SIT predictions and thin SIT estimates from MET. The intervals are of size 5 cm starting from 0 cm. Figure 7.3 illustrates the RMSE values for each interval as purple and green bar plots located in the specific interval. The green bar represents the RMSE value calculated from the thin SIT estimates from MET interval, the purple bar represents RMSE values from the thin SIT predictions interval. The first one compares the "true"[1] values within the interval to the predictions of the corresponding "true" values for each pixel, while the latter compares the predicted values within the interval to those "true" pixel values the prediction came from. This gives an idea on how well the fitted power function performs in different ranges of thin SIT. The distribution for both the predicted thin SIT values and the thin SIT estimates are also shown. As expected, the RMSE values increases with thicker sea ice due to more overlapping albedo values and performs reasonably well for very thin ice between 0 and 5cm with an RMSE value considerably lower than the overall mean calculated in table 7.1 at around 2.

Figure 7.8 represents a sub-scene from the TOA data-set with the prediction image from each fitted function, the thin SIT estimate from MET and the RGB-composite image. Each prediction image seems to represent thinner ice regions fairly reasonable, but overestimates the thickness for SIT values above 20 cm. Especially bad for the lower left region where the SIT values are much thinner than the predictions estimate. The logarithmic regression explodes to infinity

1. Quotation marks due to the SIT estimates not being the actual thickness values, but an estimate from MET

and can be seen as white pixels in figure 7.8b. There are significant errors for all fitted functions, but the fitted power function performs best qualitatively and quantitatively for the TOA data set.

7.3.2 Band reflectance, multivariate gradient boosting regression tree

The previous section gave us a good idea in how the total albedo data relate to the thin SIT estimates. However, we're only using the weighted sum of the bands and restrict ourselves to only one dimension. Utilising the band reflectance information S-2 has to offer, we can explore more thoroughly by using the selected GBM framework, LightGBM, introduced in section 7.1.2.

Three models were trained with the same parameters, one for each data-set (TOA,TOA with DOS and BOA). The data-sets were split into training and test sets, with 80/20 split respectively. The RMSE evaluation for training and test data for each model are shown in table 7.2. The training and test data result are very close, with the GBM model trained on TOA data edging out the two other models. The same can be said for the evaluation in table 7.1.

Train and test RMSE values

	BOA	DOS	TOA
Train	2.661	2.612	2.559
Test	2.710	2.653	2.618

Table 7.2: Training and test data RMSE metrics from the LightGBM models.

GBM models makes a prediction by adding together the outputs of the multiple weak models. Our trained models contains 1500 of these weak models or regression trees, making it hard to analyse the inner workings of resulting predictions. Instead of looking at each individual tree, we can look at the feature importance. Feature importance provides a score that indicates how valuable each feature was during the construction of the model. Figure 7.4 illustrates the feature importance for each band as the number of times the feature is used in the model. In the univariate model we heavily weighted the VIS band reflectances based on observations in literature and our own observations. However, the models seems to use the bands located in the SWIR regions quite extensively compared to bands in the VIS and NIR ranges. It's difficult to determine a physical reason for this as the general reflectance increase in band 11 and 12 seems reasonable with increasing SIT for the mean line, but as seen in figure 7.5 showing the reflectance standard deviation and mean line for each thickness in band 11 and 12, the reflectance values are more

spread for each SIT level.

The prediction from gradient boosted regression trees are restricted to the range of the target variable (0 to 30 cm), which is a benefit to us, because we have no data in beyond this range. This avoids the problem of omitting predictions that fall beyond 30 cm, as what happened for the univariate case. As mentioned in the previous section, the RMSE metric is biased towards the range with more SIT data points. The RMSE values for the same intervals evaluated for the GBM models are illustrated in figure 7.6. Every data-set seems to give similar results, and showing a more consistent RMSE value over the SIT range than the univariate regression models. The distribution between the predicted values and the estimated SIT values are also quite similar, giving us a sign that the predictions are much more aligned with the target data. There is a spike in RMSE value for the interval 25 to 30 cm, indicating that the models probably underestimates the SIT levels in this range.

The sub-scene predictions are illustrated in figure 7.9. It's hard to see any clear differences between the models. However, the general product looks good for SIT up to 25 cm. For SIT values above this, the models underestimates the SIT values. Qualitatively, all of the models perform essentially the same. For a closer look, figure 7.7 illustrates profile plots of the predicted SIT values from both the TOA and BOA GBM models[2] with 60 meter resolution S-2 image data as input. The profiles differ slightly, but the BOA model profile seems noticeable sharper than the TOA model profile. This is more clear in the areas where the SIT levels quickly rise and fall, BOA model generally reaches a higher SIT value. The atmosphere can be considered a noise component that covers the the whole scene, from figure 6.2b we can see that the general difference between the maximum and minimum BOA reflectance values for the bands in the VIS/NIR range are greater than for the same TOA band reflectance values in figure 6.2a. The noisy atmospheric component is removed and the resulting BOA band reflectance have a greater contrast between the min and max SIT, which again is reflected in the SIT prediction.

As the GBM models seem to perform equally well. The TOA and TOA with DOS models both results in a better RMSE metric than the BOA. Reasons for this may be the amount of features (band information) provided to the model, the models are over-fitted, or the BOA reflectances are over-/under-corrected (see section 6.2). Next chapter will discuss some of the implications of using the different models regarding reliability and validity, as well the issues with the data used for this regression analysis.

2. Due to time constraints and problems with SNAP software, I wasn't able to include the TOA with DOS profile plot.

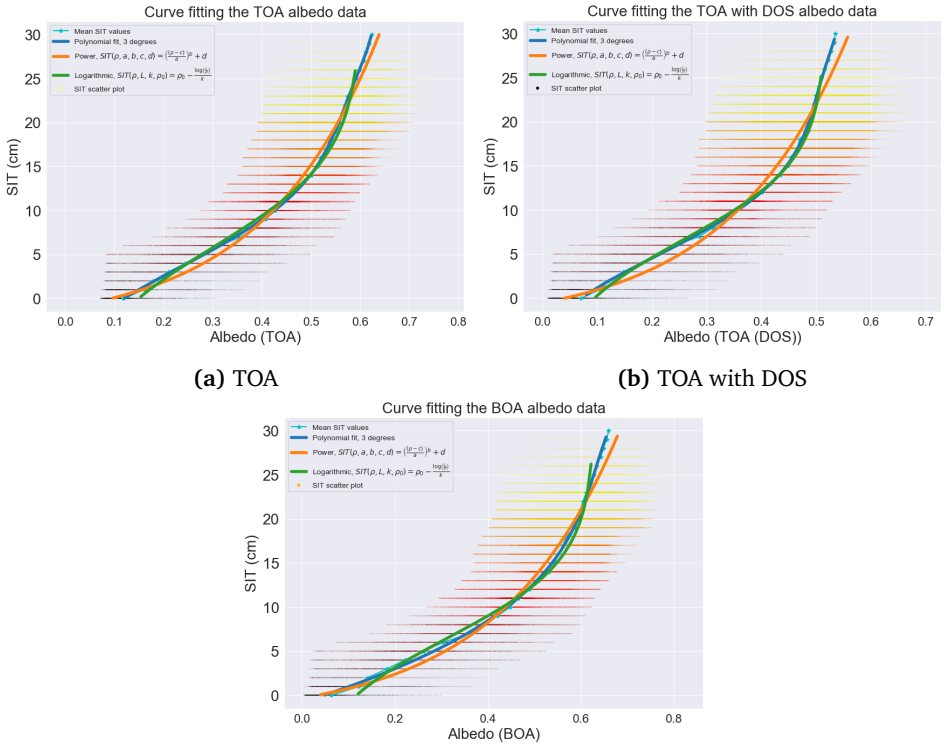

(a) TOA

(b) TOA with DOS

(c) BOA

Figure 7.2: Curve fit for every BOA, TOA and TOA with DOS applied. For our purpose of regression the axis are flipped to illustrate that we want to map from reflectance/albedo to SIT.

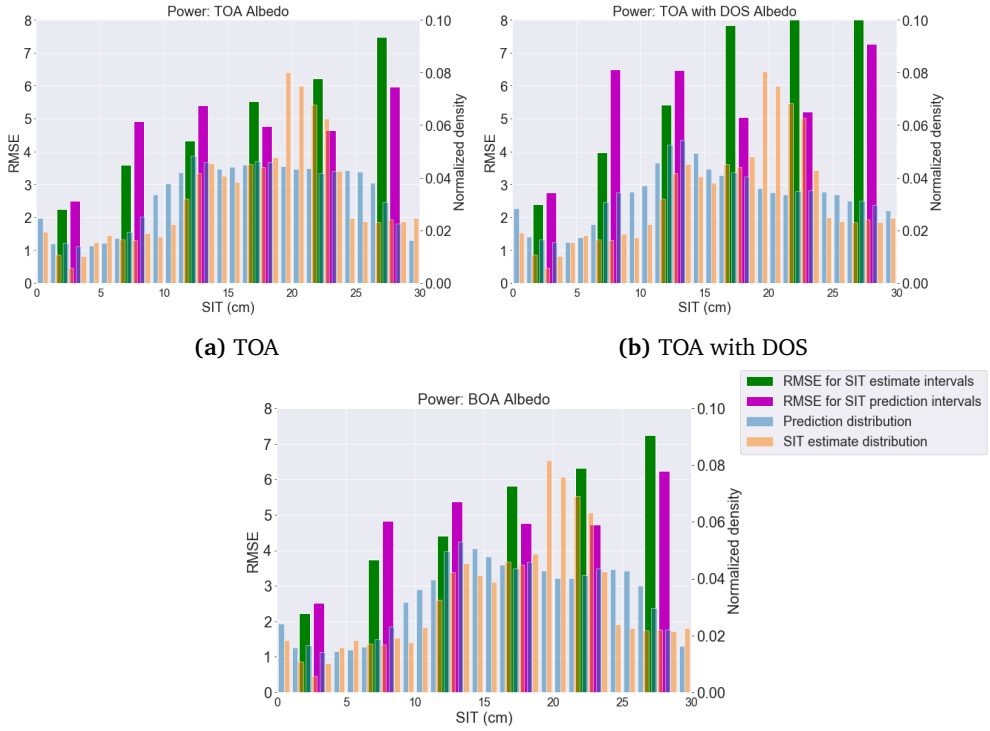

(a) TOA

(b) TOA with DOS

(c) BOA

Figure 7.3: RMSE values for specific thickness intervals in the data with the distribution of predicted SIT and the estimated SIT from MET, prediction values are from the fitted power function. The green bar represents the RMSE values calculated from the interval in the SIT estimates from MET. Purple bar represents the RMSE values from the interval in the predicted SIT values. Orange histogram is the normalized density of the SIT estimates from MET, and the blue histogram is normalized density of the predicted SIT values. Left y-axis represents the RMSE metric and right y-axis represents the normalized density.

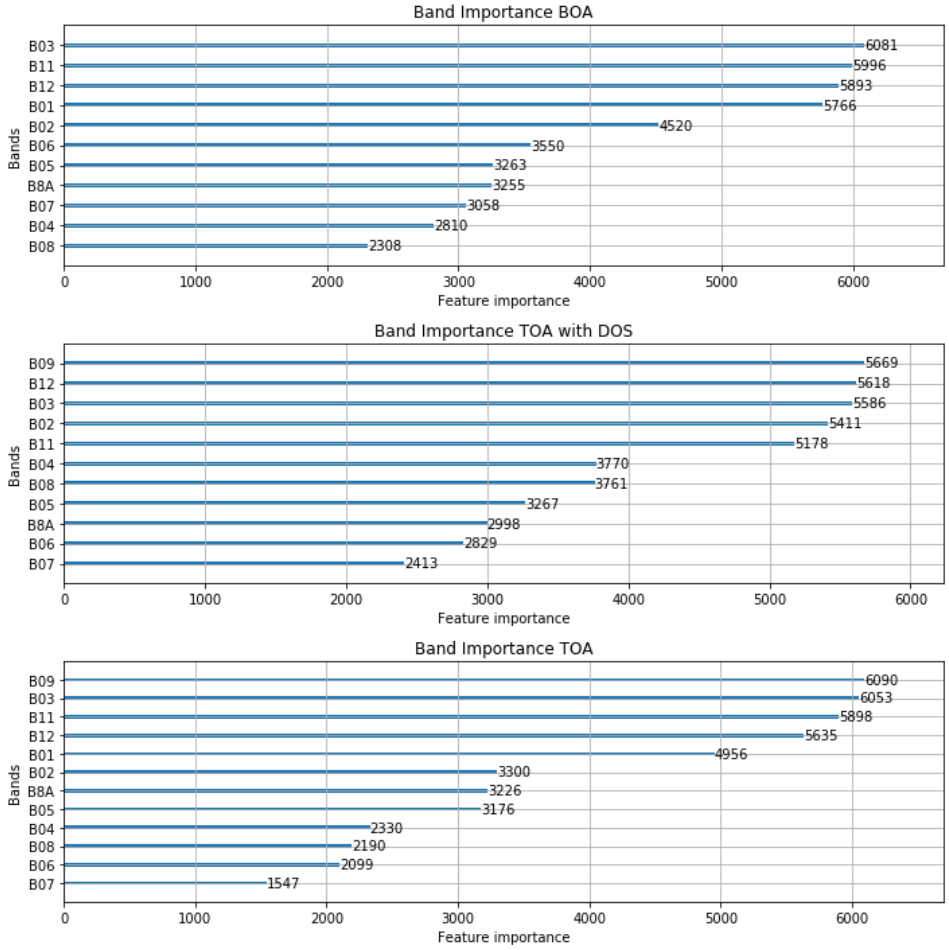

Figure 7.4: Band importance for the different GBM models

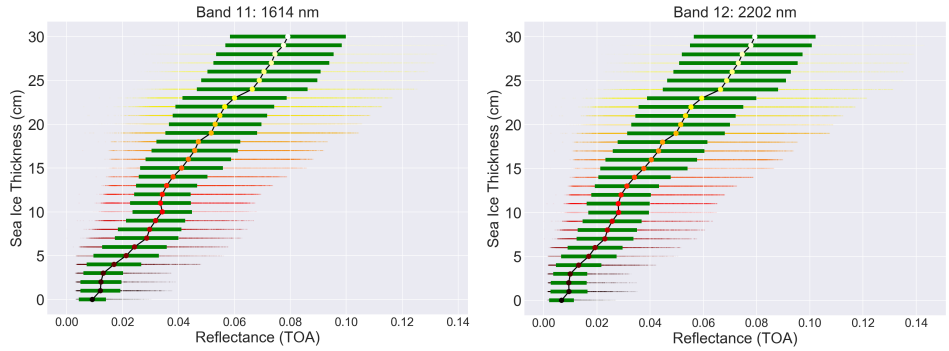

(a) **(b)**

Figure 7.5: Thin SIT as a function of TOA reflectance in band 11 and 12 (1614 and 2202 nm), green error-bars represent the standard deviation. a) TOA band 11, b) TOA band 12.

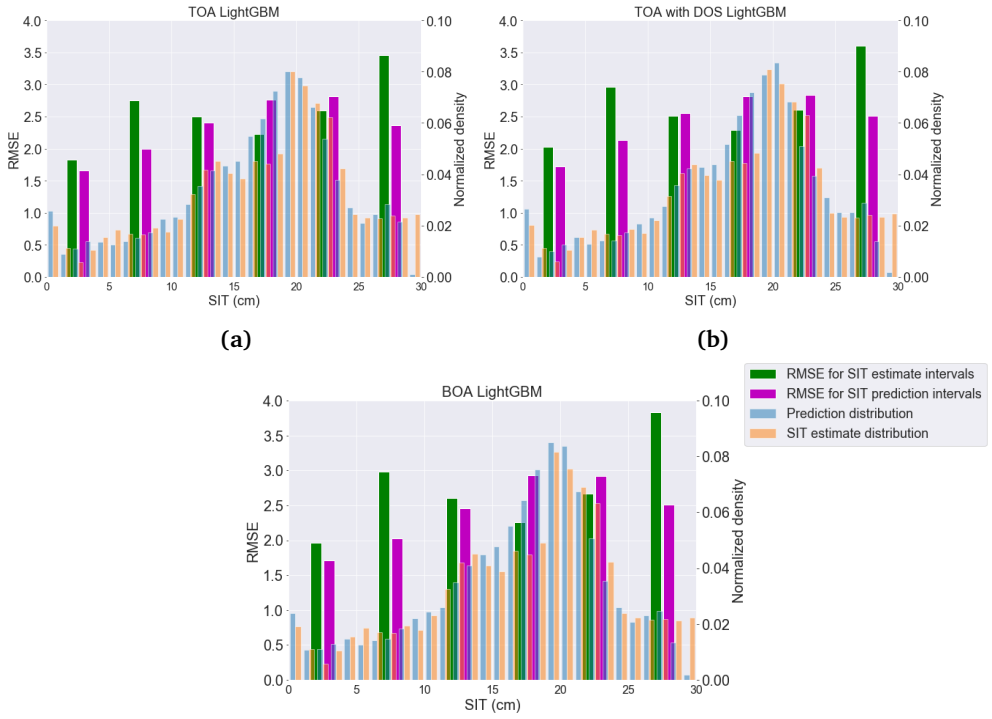

Figure 7.6: RMSE values for specific thickness intervals in the data with the distribution of predicted SIT and the estimated SIT from MET. Prediction are made from a) TOA band reflectances, b) TOA with DOS band reflectances and d) BOA band reflectances using the GBM models. Bar plots and histograms represents the same variables as in figure 7.3.

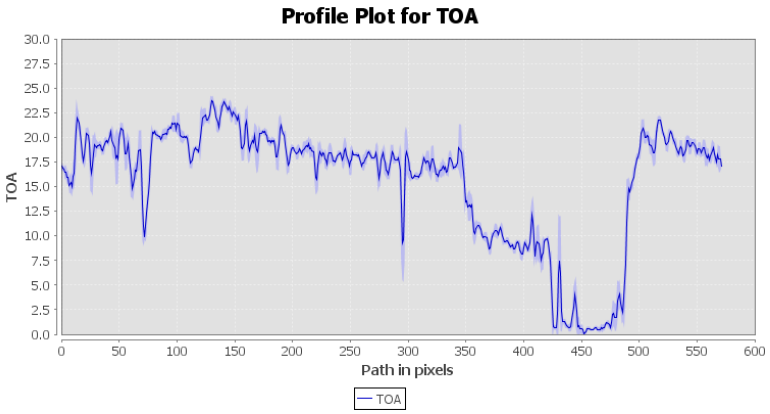

(a) Profile plot of predicted thin SIT from TOA GBM model sequence.

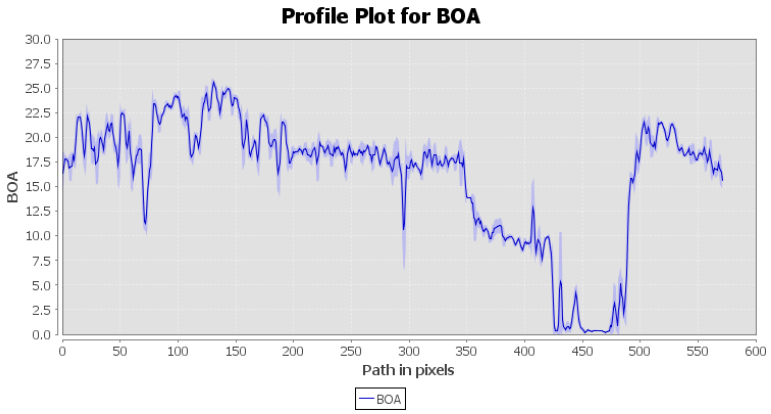

(b) Profile plot of predicted thin SIT from BOA GBM model sequence.

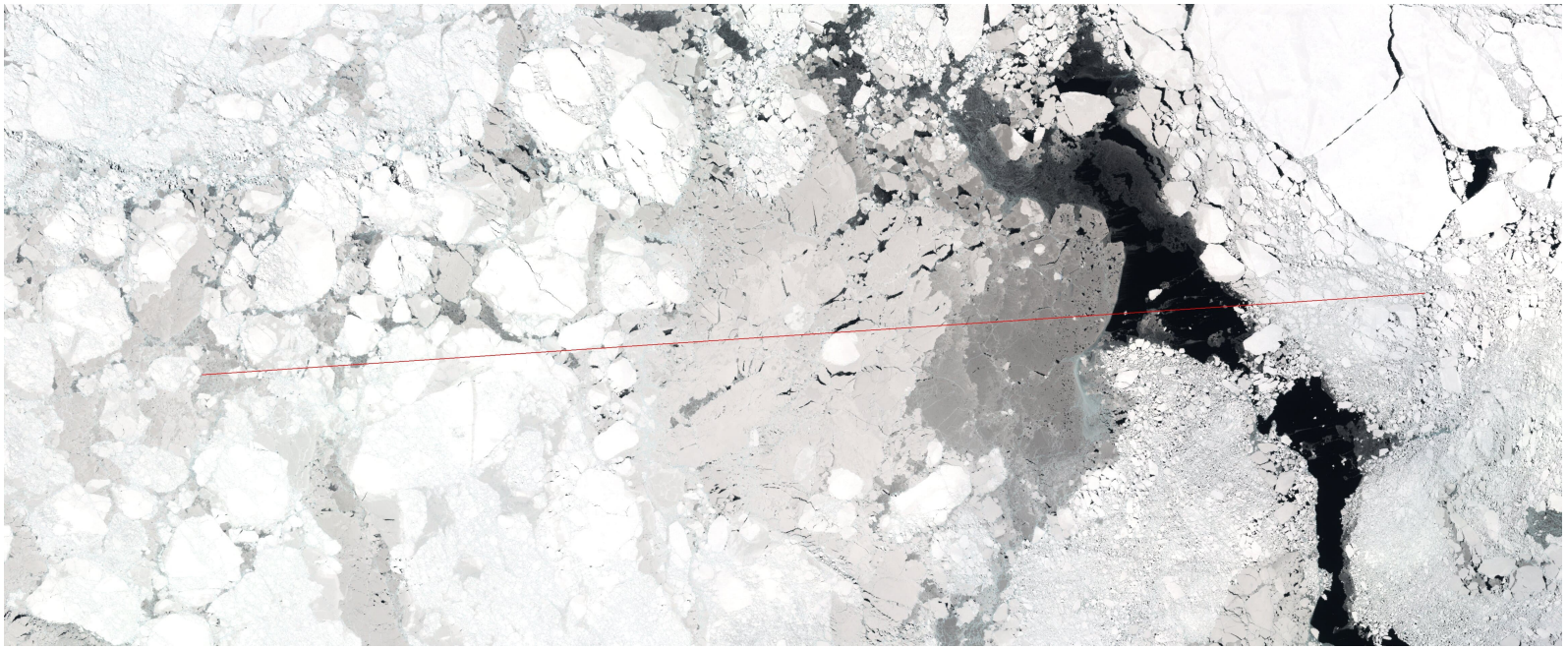

(c) RGB composite of same area, red line represents the sequence of pixels corresponding to the profile plots.

Figure 7.7: Profile plot of thin SIT predictions from the TOA and BOA GBM models.

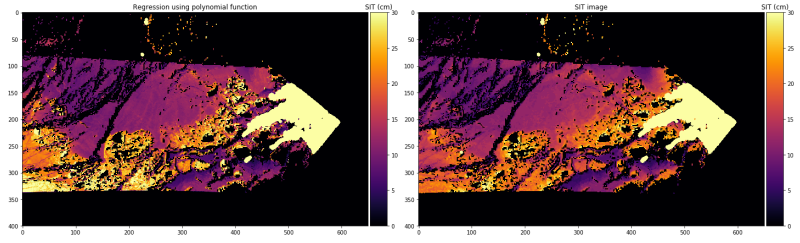

(a) SIT prediction from polynomial regression

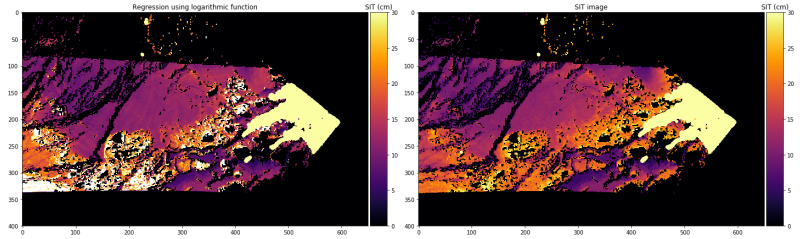

(b) SIT prediction from logarithmic regression

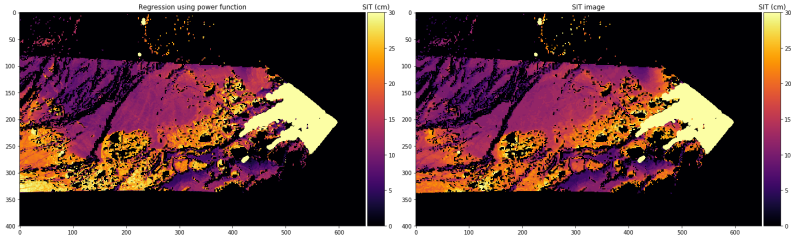

(c) SIT prediction from power function regression

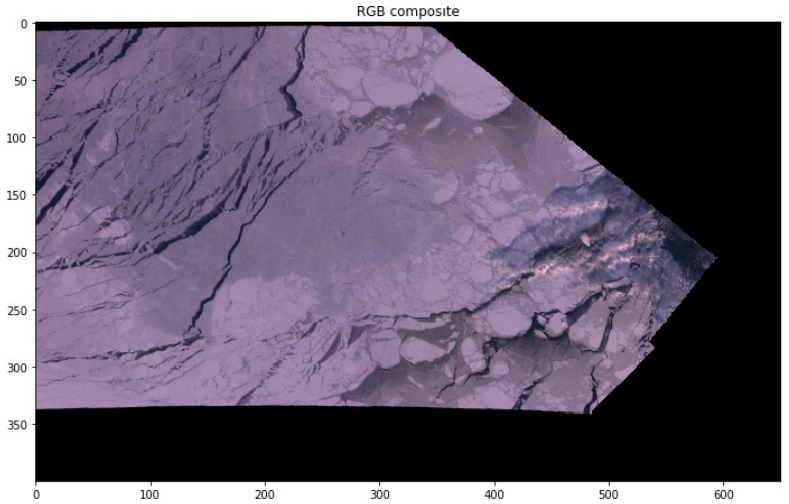

(d)

Figure 7.8: Sub-scene prediction for the different fitted functions for TOA total albedo data. Left image: Predicted thin SIT, right image: thin SIT estimate from MET, d) is the RGB composite.

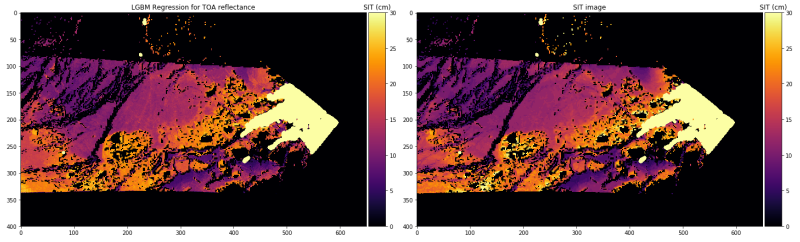

(a) SIT prediction from TOA LightGBM regression.

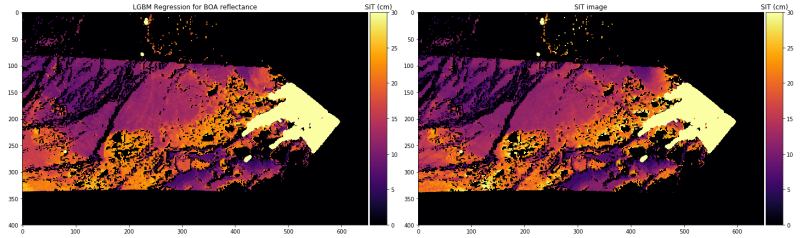

(b) SIT prediction from BOA LightGBM regression.

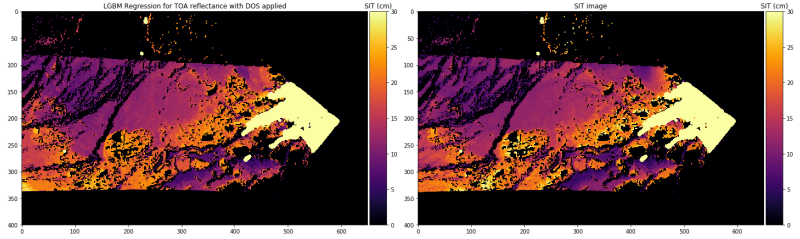

(c) SIT prediction from TOA with DOS LightGBM regression.

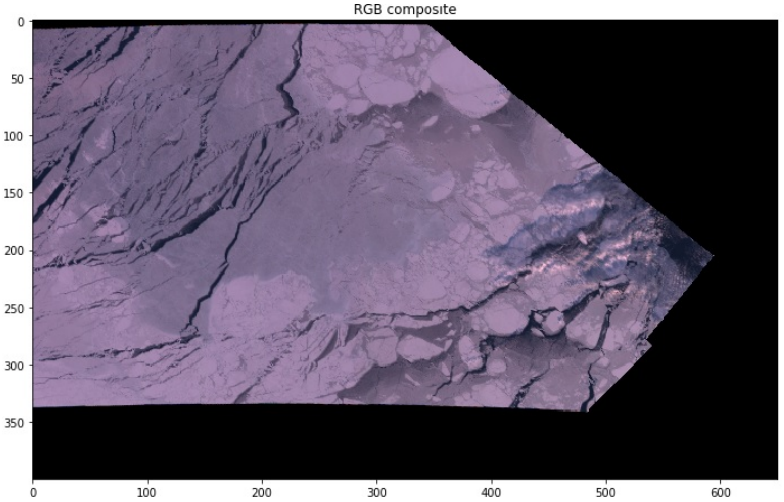

(d)

Figure 7.9: Sub-scene prediction for the different GBM models. Left image: Predicted thin SIT,right image: thin SIT estimate from MET, d) is the RGB composite.

8

Discussion and Conclusion

We have now presented several different regression results for estimating thin SIT from S-2 band reflectance data. This chapter will discuss the implications regarding the reliability of the data and the preprocessing, and how it affects the regression results. Validity of the models in relation to it's input and output will be considered and further work that needs to be done to improve the results, reliability and validity.

8.1 Reliability of the Data and Preprocessing

A regression model is only as reliable as the data it's modelled after. Discussing the problems of obtaining reliable data is important for understanding the potential solutions, further work and improvements.

The data refers to both the thin SIT image products and the corresponding S-2 band reflectance. As mentioned in section 5.1, the thin SIT retrieval algorithm was not shared due to the project is still under development at NR. We have some knowledge of the theoretical basis of the retrieval explained in section 3.2. The results and visual assessment of the relationship between the thin SIT product and band reflectance from S-2 show reasonable agreements with previous observed albedo to SIT relationship (see section 3.1 and chapter 6). We can infer from this that the thin SIT product does produce a reasonable estimate of SIT.

The reliability of the S-2 band reflectance data is dependent on many factors including, resampling, overlap/reprojection, AC and cloud/cloud-shadow masking. The thin SIT image product has a pixel resolution of 500 meters, resulting from the SLSTR instruments pixel resolution, meaning the radiation captured represent the average radiation from that spatial area of 500 meters. Taking the average before reprojecting is the most accurate and reliable method. Every overlap was visually examined, and no significant deviations between the overlapping/reprojected S-2 scenes and thin SIT product scenes were discovered. Cloud masking is always a difficult process when the majority of the underlying surface is bright ice and snow. S2Cloudless pixel detector does a reasonable job (see section 5.4.1) over sea ice surfaces, but have struggled with identifying clouds at very high solar zenith angles ($\sim 80°$), the same conditions also produce much more visible cloud shadows. This specific issue was handled in section 7.2.

The greatest concern for retrieval of reliable band reflectance data is the uncertainty due to atmospheric propagation and correcting for these effects. Sections 5.3 and 6.1 discusses some of the general and Arctic oriented problems of atmospheric propagation and the effect it has on the observed SIT spectral signatures. Assuming that a regression model, learned from TOA band reflectance data, is reliable requires the assumption of equal atmospheric conditions over space and time. Which is not a valid assumption to make. TOA data is unreliable by nature for the purposes of identifying of modelling surface properties. Section 6.2 represents the SIT BOA reflectance curves resulting from the ACOLITE AC process. The spectral relationship between the bands was found to be a better representation of the previously observed sea ice surface albedo, indicating that the BOA band reflectance is more reliable for representing the actual sea ice reflectance spectra. The question of the BOA reflectance absolute value is still a source of uncertainty and needs further investigation. The study in (König et al., 2019) also illustrated that the surface reflectance resulting from the ACOLITE processor had closest resemblance to in-situ sea ice spectra, but wasn't able to evaluate in terms of absolute intensities. The DOS process is most likely the least reliable of the processing schemes presented for the S-2 data set, as explained in section 6.3.

For our purposes of thin SIT regression model for S-2, the reliability is not only dependent on the processing and calibration but also how much variation in spatial and temporal domain is included in the data. Section 3.1 explored the highly complex nature of sea ice and the the relation between the physical and optical properties. Collecting as much seasonal and geographical variation in thin sea ice is important for producing better generalizations between S-2 band reflectance and thin SIT. This was brought up in section 5.6 as a concern because the data only includes periods in march for approximately the same

area in the Barents sea for 2018 and 2019. This doesn't necessarily mean that the regression models doesn't represent the data well, it doesn't necessarily generalize well for unseen data. There wasn't enough variation in the data to conduct a proper validation test for the regression models.

The last issue doesn't involve the data preprocessing, temporal/spatial variety or regression method. The physical layer of snow has been stressed as a major obstacle for retrieval of sea ice properties, especially SIT (see section 3.3). We assumed the snow will range from 0 to 3 cm due to the empirical relationship defined in equation 3.10, and the radiation reflected of sea ice still contributes considerably to the observed spectral albedo. Not a very safe assumption as snow depth on Arctic sea ice has varies with seasons, mostly ice free in August, accumulates rapidly in September-November, very slowly in December-January and moderately from February to May (Warren et al., 1999).

8.2 Further Work

There is further work that needs to be done to achieve a true reliable thin SIT model for S-2. Collection of data that includes seasonal and geographical variation is needed. High resolution validation data for validating performance from high resolution SIT outputs would absolutely be critical, this would most likely have to be in-situ measurements of SIT and requires a lot of work. Precise corrections for atmospheric propagation and validations of BOA reflectance retrievals for optical Arctic sea ice research, also emphasized in (Malenovskỳ et al., 2012). Cloud masking is still not optimal for Arctic conditions and can always be improved upon. As the reliability and quality of S-2 data increases, further evaluation of multivariate regression models can be properly conducted.

The thin SIT product has a thick ice mask applied for narrowing down pixels to process. The thick ice mask has not been evaluated in this thesis and future work identifying and excluding regions of thick ice should be a priority.

8.3 Conclusion and Final Product

The goal of this thesis was to achieve a reliable regression model estimating thin SIT for S-2 band reflectance information using the thin SIT product provided by MET and NR. This thesis proved a clear correlation between S-2 band reflectance and thin SIT, and that there is high certainty of the possibility of a reliable thin SIT model for the high resolution S-2 MSI instrument. There were four models, three univariate models applied to three total albedo estimation data-sets using NLLS, and one multivariate model applied to three band reflectance data-sets using a GBM framework. The best performing univariate model was the fitted power function for the TOA total albedo estimation data,

and the best performing multivariate model was the LightGBM model for the TOA band reflectance. Overall the multivariate LightGBM regression model performed the best with the lowest RMSE scores.

The reliability is an important factor for automatic monitoring of any sea ice parameter. S-2 carries a lot of potential for very high resolution coverage of Arctic sea ice. However research on this is scarce (König et al., 2019) and AC for Arctic sea ice, has not been accurately validated for absolute intensities, reliable optical reflectance data from S-2 is a difficult process and requires a lot of human intervention. A more reliable thin SIT regression model can be achieved with a greater variable data set, proper AC and high resolution in-situ validation measurements.

The thin SIT models will be released in a python script after the submission of this thesis[1]. The script will input a S-2 image file in .SAFE format and output a thin SIT raster. The user have the option to choose the processing scheme, being using TOA, BOA or DOS, and the model, being the fitted power, logarithmic or polynomial functions or the LightGBM models.

1. Will be released on GitHub (Skogvold (2019b))

A

Non-Linear Least Squares

Non-linear least squares analysis is used to fit a set of observations of size M (x_1, y_1), (x_2, y_2), ... (x_m, y_m) with a non-linear model/function with a set of unknown parameters with size n. A non-linear model is any model of the form:

$$f(x_i; \vec{\beta}) \tag{A.1}$$

where the function $f(x_i; \vec{\beta})$ is not linear with respect to its parameters $\vec{\beta} = \beta_0, \beta_1 ..., \beta_n$. We use the method of least squares to find the unknown parameters. That is finding the vector $\vec{\beta}$ such that the curve fits best given the data in sense of least squares, the sum of squared residuals

$$S = \sum_i r_i^2 \tag{A.2}$$

where

$$r = y_i - f(x_i; \vec{\beta}) \tag{A.3}$$

The minimum value of the sum of squared residuals S occurs when the gradient is zero. Because $\vec{\beta}$ contain n parameters, there are n number of gradient equations.

$$\frac{\partial S}{\partial \vec{\beta}_j} = 2 \sum_i r_i \frac{\partial r_i}{\partial \beta_j} = 0, \quad \text{for } j = 0, 1, 2, .., n \tag{A.4}$$

The parameters are initialized and optimized iteratively. At each iteration the model is linearised by a first order Taylor-polynomial expansion about β_k. The

linearised model is approximated by

$$f(x_i;\vec{\beta}) \simeq f(x_i;\vec{\beta}^k) + \sum_j \frac{\partial f(x_i;\vec{\beta}^k)}{\partial \beta_j}(\beta_j - \beta_j^k) \tag{A.5}$$

Where k is the iteration number. We can write the above equation on terms of sum of components of the Jacobian matrix $\boldsymbol{J}_{ij} = \frac{\partial f(x_i;\beta^k)}{\partial \beta_j^k}$,

$$f(x_i;\vec{\beta}) \simeq f(x_i;\vec{\beta}^k) + \sum_j \boldsymbol{J}_{ij}\Delta\beta_j \tag{A.6}$$

The residuals are given by denoting that $\frac{\partial r_i}{\partial \beta_j} = -\frac{\partial f(x_i;\vec{\beta})}{\partial \beta_j} = -\boldsymbol{J}_{ij}$

$$\begin{aligned} \Delta y_i &= y_i - f(x_i;\vec{\beta}^k) \\ r_i &\simeq \Delta y_i - \sum_{s=1}^{n} \boldsymbol{J}_{is}\Delta\beta_s \end{aligned} \tag{A.7}$$

Substituting back into equation A.4 and rearranging,

$$\sum_{i=1}^{M}\sum_{s=1}^{n} \boldsymbol{J}_{ij}\boldsymbol{J}_{is}\Delta\beta_s = \sum_{i=1}^{M} \boldsymbol{J}_{ij}\Delta y_i, \quad \text{for } j = 0, 1, 2, \ldots n \tag{A.8}$$

These are n simultaneous equations.

Bibliography

American Society for Testing and Materials. Committee E21 on Space Simulation and Applications of Space Technology. *Standard Solar Constant and Zero Air Mass Solar Spectral Irradiance Tables*. ASTM International, 2000.

C. E. Barnett. Some applications of wave-length turbidimetry in the infrared. *The Journal of Physical Chemistry*, 46(1):69–75, 1942. doi: 10.1021/j150415a009. URL https://doi.org/10.1021/j150415a009.

Pat S Chavez Jr. An improved dark-object subtraction technique for atmospheric scattering correction of multispectral data. *Remote sensing of environment*, 24(3):459–479, 1988.

Wikimedia Commons. File:atmosfaerisk spredning.png — wikimedia commons, the free media repository, 2017. URL https://commons.wikimedia.org/wiki/File:Atmosfaerisk_spredning.png. [Online; accessed 4-May-2019].

Gordon FN Cox and Wilford F Weeks. Salinity variations in sea ice. *Journal of Glaciology*, 13(67):109–120, 1974.

Yu P Doronin. On a method of calculating the compactness and drift of ice floes. *AIDJEX Bull*, 3:22–29, 1971.

ESA. Sentinel-2 spectral response functions (s2-srf). https://earth.esa.int/web/sentinel/user-guides/sentinel-2-msi/document-library/-/asset_publisher/Wk0TKajiISaR/content/sentinel-2a-spectral-responses, 2017.

A Gatti and A Galoppo. Sentinel-2 products specification document. *Available online (accessed March, 2018) https://sentinel.esa.int/documents/247904/685211/Sentinel-2-Products-Specification-Document*, 2018.

GDAL/OGR contributors. *GDAL/OGR Geospatial Data Abstraction software Library*. Open Source Geospatial Foundation, 2018. URL http://gdal.org.

Sean Gillies et al. Rasterio: geospatial raster i/o for Python programmers, 2013–. URL https://github.com/mapbox/rasterio.

Thomas C Grenfell. A theoretical model of the optical properties of sea ice in the visible and near infrared. *Journal of Geophysical Research: Oceans*, 88 (C14):9723–9735, 1983.

Thomas C. Grenfell and Gary A. Maykut. The optical properties of ice and snow in the arctic basin. *Journal of Glaciology*, 18(80):445–463, 1977. doi: 10.3189/S0022143000021122.

Eric Jones, Travis Oliphant, Pearu Peterson, et al. SciPy: Open source scientific tools for Python, 2001–. URL http://www.scipy.org/. [Online; accessed March 15, 2019].

Guolin Ke, Qi Meng, Thomas Finley, Taifeng Wang, Wei Chen, Weidong Ma, Qiwei Ye, and Tie-Yan Liu. Lightgbm: A highly efficient gradient boosting decision tree. In *Advances in Neural Information Processing Systems*, pages 3146–3154, 2017.

Lauren E Kipp, Matthew A Charette, Willard S Moore, Paul B Henderson, and Ignatius G Rigor. Increased fluxes of shelf-derived materials to the central arctic ocean. *Science advances*, 4(1):eaao1302, 2018.

Marcel König, Martin Hieronymi, and Natascha Oppelt. Application of sentinel-2 msi in arctic research: Evaluating the performance of atmospheric correction approaches over arctic sea ice. *Frontiers in Earth Science*, 7:22, 2019. ISSN 2296-6463. doi: 10.3389/feart.2019.00022. URL https://www.frontiersin.org/article/10.3389/feart.2019.00022.

Zbyněk Malenovskỳ, Helmut Rott, Josef Cihlar, Michael E Schaepman, Glenda García-Santos, Richard Fernandes, and Michael Berger. Sentinels for science: Potential of sentinel-1,-2, and-3 missions for scientific observations of ocean, cryosphere, and land. *Remote Sensing of Environment*, 120:91–101, 2012.

C Melsheimer, M Mäkynen, TS Rasmussen, Ø Rudjord, M Similä, R Solberg, and NP Walker. Comparison and validation of four arctic sea ice thickness products of the ec polar ice project. In *Living Planet Symposium*, volume 740, page 340, 2016.

Microsoft. Lightgbm documentation. https://lightgbm.readthedocs.io/en/latest/index.html, 2017.

Donald K Perovich. The optical properties of sea ice. Technical report, COLD

REGIONS RESEARCH AND ENGINEERING LAB HANOVER NH, 1996.

Donald K. Perovich, Collin S. Roesler, and W. Scott Pegau. Variability in arctic sea ice optical properties. *Journal of Geophysical Research: Oceans*, 103(C1):1193–1208, 1998. doi: 10.1029/97JC01614. URL https://agupubs.onlinelibrary.wiley.com/doi/abs/10.1029/97JC01614.

R Richter and D Schläpfer. Atmospheric/topographic correction for satellite imagery (atcor-2/3 user guide, version 8.3. 1, february 2014). *ReSe Applications Schläpfer Langeggweg*, 3, 2013.

R Richter, J Louis, and U Müller-Wilm. S2-pdgs-mpc-l2a-sum-v2.5. *Sen2Cor Software Release Note*, pages 13–16, 2018.

Øystein Rudfjord, Øivind T.D Trier, and Rune Solberg. Retrieval of thin sea ice thickness from thermal optical data. *NR-notat SAMBA/27/11*, page 50, 2011.

K. P. Shine and A. Henderson-Sellers. The sensitivity of a thermodynamic sea ice model to changes in surface albedo parameterization. *Journal of Geophysical Research*, 90(D1):2243–2250, 1985. ISSN 0148-0227. doi: 10.1029/JD090iD01p02243.

Sinergise and Matej Aleksandrov. Sentinel hub cloud detector: s2cloudless, sentinel hub cloud detector for sentinel-2 images in python. https://github.com/sentinel-hub/sentinel2-cloud-detector, 2018. Accessed: 2018-15-Nov.

Øystein F. Skogvold. S2pixeloverlap: Sentinel-2 pixel overlap v0.7 (unstable). https://doi.org/10.5281/zenodo.2652433 , 2019a.

Øystein F. Skogvold. Øystein skogvold github. https://github.com/oyssko , 2019b.

D. O. Staley and G. M. Jurica. Effective atmospheric emissivity under clear skies. *Journal of Applied Meteorology*, 11(2):349–356, 1972. doi: 10.1175/1520-0450(1972)011<0349:EAEUCS>2.0.CO;2. URL https://doi.org/10.1175/1520-0450(1972)011<0349:EAEUCS>2.0.CO;2.

Quinten Vanhellemont and Kevin Ruddick. Acolite for sentinel-2: Aquatic applications of msi imagery. In *Proceedings of the 2016 ESA Living Planet Symposium, Prague, Czech Republic*, pages 9–13, 2016.

Quinten Vanhellemont and Kevin Ruddick. Atmospheric correction of metre-scale optical satellite data for inland and coastal water applications. *Remote*

Sensing of Environment, 216:586–597, 2018.

Silvia Vanino, Pasquale Nino, Carlo De Michele, Salvatore Falanga Bolognesi, Guido D'Urso, Claudia Di Bene, Bruno Pennelli, Francesco Vuolo, Roberta Farina, Giuseppe Pulighe, et al. Capability of sentinel-2 data for estimating maximum evapotranspiration and irrigation requirements for tomato crop in central italy. *Remote sensing of environment*, 215:452–470, 2018.

Stephen G. Warren, Ignatius G. Rigor, Norbert Untersteiner, Vladimir F. Radionov, Nikolay N. Bryazgin, Yevgeniy I. Aleksandrov, and Roger Colony. Snow depth on arctic sea ice. *Journal of Climate*, 12(6):1814–1829, 1999. doi: 10.1175/1520-0442(1999)012<1814:SDOASI>2.0.CO;2. URL https://doi.org/10.1175/1520-0442(1999)012<1814:SDOASI>2.0.CO;2.

Warren J Wiscombe and Stephen G Warren. A model for the spectral albedo of snow. i: Pure snow. *Journal of the Atmospheric Sciences*, 37(12):2712–2733, 1980.

Y Yu and DA Rothrock. Thin ice thickness from satellite thermal imagery. *Journal of Geophysical Research: Oceans*, 101(C11):25753–25766, 1996.

Anze Zupanc. Improving cloud detection with machine learning, December 2017. URL https://medium.com/sentinel-hub/improving-cloud-detection-with-machine-learning-c09dc5d7cf13. Accessed: 2018-15-nov.